ACS EARTH AND SPACE CHEMISTRY

http://pubs.acs.org/journal/aesccq

Article

Humidity-Dependent Viscosity of Secondary Organic Aerosol from Ozonolysis of β-Caryophyllene: Measurements, Predictions, and Implications

Adrian M. Maclean, Natalie R. Smith, Ying Li, Yuanzhou Huang, Anusha P. S. Hettiyadura, Giuseppe V. Crescenzo, Manabu Shiraiwa, Alexander Laskin, Sergey A. Nizkorodov,* and Allan K. Bertram*

Cite This: *ACS Earth Space Chem.* 2021, 5, 305−318

Read Online

ACCESS | Metrics & More | Article Recommendations | Supporting Information

ABSTRACT: To predict important secondary organic aerosol (SOA) properties, information on viscosity or diffusion rates within SOA is needed. Ozonolysis of β-caryophyllene is an important SOA source; however, very few viscosity or diffusion rate measurements have been performed for this SOA type and none as a function of relative humidity (RH). In this study, we measured viscosity as a function of RH for SOA generated from the ozonolysis of β-caryophyllene using the poke-flow technique. At an RH of 0 and 48%, the viscosity was between 6.9×10^5 and 2.4×10^7 Pa s, and between 1.3×10^3 and 5.6×10^4 Pa s, respectively. Based on these viscosities and the fractional Stokes−Einstein equation, characteristic mixing timescales of organics within 200 nm β-caryophyllene SOA particles range from ∼0.2 h at 0% RH to <3 s at 48% RH, suggesting that these particles should be well-mixed under most conditions in the lower atmosphere. The chemical composition of the SOA was also determined using nano-desorption electrospray ionization mass spectrometry. The measured chemical composition and the method of DeRieux et al. (*ACP*, 2018) were used to predict the viscosity of β-caryophyllene SOA. If the mass spectra peak abundances were adjusted to account for the sensitivity of the electrospray ionization to larger molecular weight components, the predicted viscosity overlapped with the measured viscosity at 0% RH, while the predicted viscosities at 15−48% RH were slightly higher than the measured viscosities. The measured viscosities also overlapped with viscosity predictions based on a simple mole-fraction based Arrhenius mixing rule.

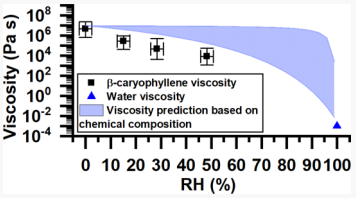

KEYWORDS: *viscosity, secondary organic aerosol, sesquiterpene, β-caryophyllene, mixing time, mass spectrometry*

1. INTRODUCTION

Secondary organic aerosol (SOA) is formed in the atmosphere when volatile organic compounds (VOCs) from biogenic and anthropogenic sources are oxidized followed by partitioning of the reaction products to the particle phase[1] or multiphase reactions of the oxidation products.[2] On a global scale, biogenic VOCs are the dominant contributors to SOA.[1,3,4] The three main classes of biogenic VOCs important for SOA formation are isoprene, monoterpenes, and sesquiterpenes.[4] A recent modeling study showed that the global burden of SOA increased by 48% relative to the base case when sesquiterpenes were included in the model.[5] Field measurements and modeling studies have also illustrated that sesquiterpenes can contribute significantly to atmospheric SOA.[6−9] Examples of atmospherically relevant sesquiterpenes include β-caryophyllene, α-cedrene, α-humulene, and longifolene.[10,11]

SOA is important because it can impact the Earth's climate directly, by scattering incoming solar radiation, and indirectly, by serving as nuclei for cloud droplets and ice crystals.[12−15] SOA can also impact air quality by reducing visibility and negatively impacting health.[16−18] To predict important properties of SOA in the atmosphere, information on the diffusion rates of organics within SOA is needed. For example, diffusion rates of organics within particles affect the mass and size distribution of SOA[19−26] and the long-range transport of pollutants such as polycyclic aromatic hydrocarbons in the atmosphere.[27−31] In addition, diffusion rates can affect rates and mechanisms of photochemical and multiphase reactions within SOA.[19,32−41]

Diffusion rates of organics within SOA or SOA proxies have been determined in some studies by tracking the diffusion of fluorescent probe molecules within SOA or their proxies[42−46] and by measuring of evaporation rates of organic molecules from SOA or SOA proxies.[27,47−49] In cases where diffusion rates of organics have not been measured, they can be estimated from viscosity measurements using the Stokes−Einstein equation[43,48,50−52] or the fractional Stokes−Einstein equation.[43,44,48] A challenging aspect of measuring diffusion rates and viscosity

Received: October 27, 2020
Revised: December 22, 2020
Accepted: December 29, 2020
Published: January 15, 2021

within SOA is the low amount of material available for experiments, which precludes the use of traditional methods.[53]

Recently, Shiraiwa et al.,[54] DeRieux et al.,[55] Gervasi et al.,[56] and Li et al.[57] developed methods for predicting the viscosities of SOA from its chemical composition, which can be used with chemical transport models to predict viscosity of atmospheric SOA.[54,58] These methods have been used to predict the viscosity and glass transition temperatures of several types of SOA (isoprene SOA, α-pinene SOA, toluene SOA, and ambient SOA).[26,55,56,59−65] However, the accuracy of these methods for predicting the viscosity of SOA has only been tested in a few cases, and the accuracy of these methods has never been tested for sesquiterpene SOA.

The viscosity of SOA as a function of RH can also be predicted using mixing rules and measured viscosities of water and dry SOA.[56,66−68] Gervasi et al.[56] showed that a mole-fraction based mixing rule is the best choice among simple mixing rules for predicting viscosity in a binary aqueous system. However, the accuracy of mixing rules for predicting the viscosity of SOA as a function of RH has only been tested in a few cases.[56,67,68]

Only two studies have reported diffusion rates or viscosities within sesquiterpene SOA. Zhao et al.[49] measured a diffusion coefficient of 3×10^{-19} m^2 s^{-1} under dry conditions of 2-ethylhexyl nitrate within SOA generated from α-cedrene ozonolysis. Champion et al.[69] measured viscosities under dry conditions of SOA generated from β-caryophyllene photooxidation. What is currently missing are measurements of diffusion rates or viscosities within sesquiterpene SOA as a function of relative humidity (RH). Such RH-dependent measurements are critical, since RH varies from 0 to over 100% in the atmosphere and viscosity and diffusion rates have a strong dependence on RH.[70]

To address the knowledge gaps mentioned above, we measured viscosity as a function of RH for SOA generated via ozonolysis of β-caryophyllene (see Figure 1 for the chemical structure of β-caryophyllene). The measured viscosities and the fractional Stokes−Einstein relation were used to estimate characteristic mixing timescales of organic molecules within β-caryophyllene SOA for typical RH conditions found in the planetary boundary layer (the region of the atmosphere between the Earth's surface and approximately 1 km in height). In addition to measuring viscosity, we also measured the chemical composition of the SOA using high-resolution mass spectrometry with three different types of direct-infusion ionization sources. The chemical composition and the measured RH-dependent viscosities for β-caryophyllene SOA were used to test the accuracy of the parameterization from DeRieux et al.[55] for predicting viscosities of β-caryophyllene SOA. Finally, we evaluated the ability of a simple mole-fraction based Arrhenius mixing rule to predict the viscosity of the β-caryophyllene SOA as a function of RH from knowledge of the viscosity of water and the dry SOA.

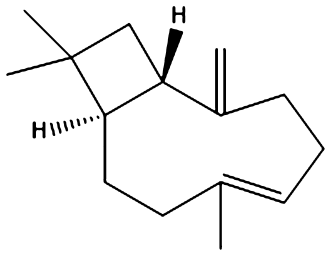

Figure 1. Chemical structure of β-caryophyllene.

2. EXPERIMENTAL SECTION

2.1. SOA Generation. SOA was generated in an environmental chamber at the University of British Columbia via dark ozonolysis of β-caryophyllene. The chamber was based on the design by Parsons et al.[71] and consisted of a 1.8 m^3 Teflon bag (Ingeniven) housed in a reflective aluminum enclosure (Figure S1). The enclosure had 24 UV lights (40 W Sylvania black lights, peak UV wavelength of ∼360 nm) mounted on the inside of the enclosure for photochemical studies; however, the lamps were not used in the current study except for cleaning the Teflon bag. The chamber bag was periodically cleaned by passing dry air, ozone (1.2 ppm), and water vapor through the chamber with the UV lights on. Particles were continuously generated and collected by running the environmental chamber in a continuous-flow mode, similar to other continuous-flow environmental chambers.[72−75] The flow rate into and out of the chamber was ∼18.2 L min^{-1}, resulting in a calculated residence time of 1.7 h, consistent with residence time measurements (Figure S2).

A zero-air generator (Aadco 737) provided dry and hydrocarbon-free air for SOA generation. The RH of the air from the generator was <1% based on measurements with a humidity meter (Vaisala HMT 330). Ozone was generated externally to the chamber by flowing 0.5−1 L min^{-1} of the dry air through an ozone generator (Jelight 600). A mixture of 2 wt % β-caryophyllene (Sigma-Aldrich, ≥98%) was prepared in 2-butanol (Sigma-Aldrich, ≥99% purity) and the resulting solution was continuously added (flow rate of 25 μL h^{-1}) with a syringe pump (Cole-Parmer model 100) to a round-bottom flask heated to 110 °C. A flow of 17.2−17.7 L min^{-1} of the dry air was passed through the heated flask and carried the β-caryophyllene and 2-butanol vapors into the chamber. The 2-butanol was added to the chamber as a scavenger of OH radicals, which can be produced during some reaction pathways for the ozonolysis of β-caryophyllene.[76] The 2-butanol was estimated to scavenge ∼84% of OH radicals produced in the chamber based on the reaction rates of OH with 2-butanol and β-caryophyllene (Supporting Information, Section S1).

Ozone and β-caryophyllene entered the chamber through two separate 0.63 cm (outer diameter) tubes that had exits ∼0.2 cm apart within the chamber to facilitate mixing. The concentrations of ozone and β-caryophyllene flowing into the chamber were 400−1200 and 40 ppb, respectively. After SOA formation, aerosols exited the chamber through a 0.63 cm (outer diameter) tube ∼1 m away from the chamber inlets. Part of the exit flow was sampled with an ozone detector (49i, Thermo Scientific, USA). The remaining flow passed through an ozone denuder (Ozone Solutions, ODS-1) and was sampled with either an impactor to collect material for the viscosity and mass spectrometry measurements or with a scanning mobility particle sizer (SMPS) (TSI 3080 DMA and 3782 CPC) to measure the number-diameter distribution of the SOA. From the number-diameter distribution and an assumed SOA density of 990 kg m^{-3},[77] the mass concentration of the SOA in the chamber was 50−60 μg m^{-3}.

To collect SOA for viscosity or mass spectrometry measurements, the flow was sampled with a multiorifice single-stage impactor (MSP Corporation) operated at a constant flow rate of 15 L min^{-1} and a cut size below 0.18 μm (aerodynamic particle diameter). The sample collection time ranged from 16 to 24 h,

https://dx.doi.org/10.1021/acsearthspacechem.0c00296
ACS Earth Space Chem. 2021, 5, 305−318

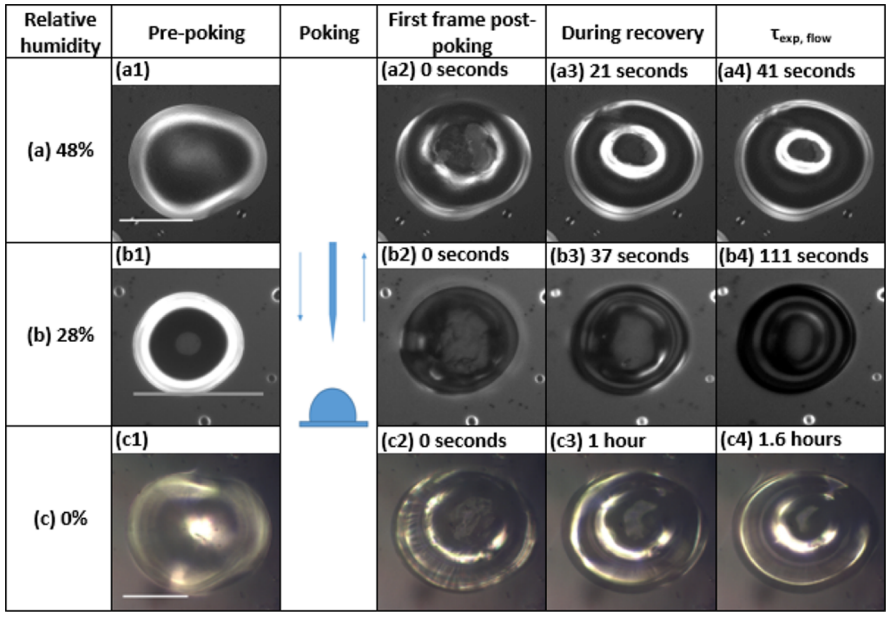

Figure 2. Optical images of particles taken during poke-flow experiments at RH values of (a) 48, (b) 28, and (c) 0%. Images [a(1),b(1),c(1)] correspond to images taken before the particle was poked. Images [a(2),b(2),c(2)] are images taken immediately after poking. Images [a(3),b(3),c(3)] are taken during recovery and images [a(4),b(4),c(4)] are taken at $\tau_{exp,flow}$ where the equivalent area diameter of the hole has decreased to 50% of its original size. The white scale bar in the prepoking images corresponds to 50 μm. The circle in the center of the particle in [b(1)] is an optical effect due to the hemispherical shape.

resulting in 0.7−1 mg of SOA collected per sample, assuming 100% collection efficiency. For the viscosity measurements, SOA was collected on fluorinated glass coverslips coated with Trichloro (1*H*,1*H*,2*H*,2*H*-perfluorooctyl) silane or FluoroPel 800 (Cytonix USA). For mass spectrometry measurements, SOA was collected on PTFE filters (47 mm, Whatman).

2.2. Measurements of Particle Viscosity. The poke-flow technique was used along with fluid simulations to determine the viscosity of the collected SOA material at room temperature (292−294 K). This technique, which is based, in part, on early experiments by Murray et al.,[78] has been described and validated by Renbaum-Wolff et al.[79] and Grayson et al.[80] For these experiments, the slides containing the SOA from the environmental chamber were mounted in a flow cell coupled to an optical microscope (Figure S3). The RH within the flow cell was controlled with a humidified flow of ultrapure N_2 (0.25−0.80 L min^{-1}). The RH was measured with a chilled mirror hygrometer (General Eastern model D-2), which was calibrated by measuring the deliquescence relative humidity of ammonium sulphate (80% RH based on Martin)[81] and potassium carbonate (43% RH based on Greenspan).[82]

In the poke-flow experiments, the particles were poked with a needle (RS-6063, Roboz Surgical Store or 13561-20, Ted Pella Company) attached to a micromanipulator. The needle was coated with a hydrophobic film (Dursan coatings, SilcoTek USA or Oilslip 110, Cytonix) to prevent SOA material from sticking to the needle. The micromanipulator allowed the needle to be moved in the *x*, *y*, and *z* direction. Prior to poking with the needle, the SOA particles had a spherical-cap geometry. After poking, the SOA material had a half-torus geometry and slowly flowed to reduce its total surface energy (e.g., Figure 2). From images recorded during the poke-flow experiments, we determined the experimental flow time, $\tau_{exp,flow}$, defined as the time taken for the equivalent area diameter of the hole in the half-torus geometry to decrease to 50% of its original diameter. The equivalent area diameter of the hole in the half-torus geometry was calculated using the following formula:[83] $d = (4A/\pi)^{1/2}$, where d is the equivalent area diameter of the hole with area A, determined from the images using Zen software (Zeiss) or ImageJ.[84]

Prior to poking the SOA particles, the particles were conditioned to the surrounding RH for 3−5, 5−25, 20, and 2−22 h for RH values of 48, 28, 15, and 0%, respectively (Table S1). These conditioning times were a factor of 0.18−22 greater than the estimated mixing times of water within the SOA (Supporting Information S2 and Table S1). Viscosities were not dependent on the conditioning times used (Figure S4). Based on this information, we assume that the SOA was near equilibrium with the gas-phase water vapor prior to poking the particles for the viscosity measurements.

When the particles were conditioning to the surrounding RH, semivolatile organic material could evaporate from the particles, potentially leading to a change in the viscosity of the particles.[25,85,86] To determine if evaporation of semivolatile organic material was important in the poke-flow experiments, a newly collected SOA sample was added to the flow cell discussed above and exposed to a dry flow of N_2 gas (0.25 L min^{-1}) for 24 h, and images were recorded every hour to quantify evaporation of the SOA particles. In this experiment, the maximum change in the 2-D projected area of the SOA particles was $-1.4 \pm 0.4\%$ (Figure 3). We conclude that the composition change due to evaporation during the poke-flow experiments was minimal. This is consistent with expectations since the volume of N_2 gas exposed to the particles in the poke-flow experiments ($\lesssim 1.2 \times 10^3$ L) was small compared to the volume of air sampled from the environmental chamber when collecting SOA for the poke-flow experiments (1.6×10^4 to 2.4×10^4 L).

The $\tau_{exp,flow}$ values determined in the poke-flow experiments were converted to viscosities using fluid simulations of the SOA material. The fluid simulations were carried out with the Microfluidics Module (version 5.2a) within COMSOL. Details are described in Grayson et al.[87] In short, the flow of the SOA

https://dx.doi.org/10.1021/acsearthspacechem.0c00296
ACS Earth Space Chem. 2021, 5, 305−318

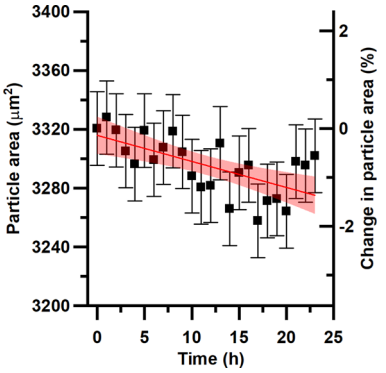

Figure 3. Particle 2-D projected area as a function of time during exposure to dry nitrogen flow with a secondary *y*-axis showing the percent change in the projected particle area. The *y*-error bars correspond to the uncertainty in the measurement of the particle area in μm^2. The straight line is a linear fit to the data and the shaded regions are the 95% confidence intervals for that fit.

material was simulated using a laminar two-phase flow with a moving mesh consisting of ~5800 elements. The simulations took into account the Navier−Stokes equation and the surface tension of the SOA. Flow occurred in the simulations to minimize the total surface energy of the system, similar to the experiments. The initial geometry in the simulations was a half-torus geometry (Figure S5a), consistent with the experiments. In the simulations, conservative values for contact angle, surface tension of the SOA, slip length (a measure of the resistance to flow at the fluid−solid interface), and density of the SOA were used (Table S2). From each simulation, a modeled flow time, $\tau_{model,flow}$, was determined, which is the time taken for the diameter of the hole in the half-torus geometry to decrease to 50% of its original value (consistent with the definition of $\tau_{exp,flow}$). To determine viscosities from $\tau_{exp,flow}$, the viscosity used in the simulation was varied until $\tau_{model,flow}$ was within ~1% of $\tau_{exp,flow}$.

2.3. Measurements of the Chemical Composition of SOA Using Mass Spectrometry. High-resolution mass spectrometry data of the collected samples were obtained in the positive and negative ion mode separately using nano-desorption electrospray ionization (nano-DESI),[88] nano-electrospray ionization (nano-ESI), and electrospray ionization (ESI) sources attached to a Q-Exactive HF-X Orbitrap mass spectrometer (Thermo Scientific) with a mass resolution of ~1.7×10^5 at m/z 400. Data were acquired from 80 to 1200 m/z in the full scan mode. A low mass calibration was performed prior to analysis using commercial mass calibration solutions (Thermo scientific, PI-88323 and PI-88324) in both positive (+) and negative (−) ion modes, separately. A spray voltage of (+ or −) 3.5 kV, a funnel RF level of 80, and a capillary temperature of 250 °C were used in all ionization modes. Samples were delivered using a syringe pump at 1 μL min^{-1} (nano-DESI), 2 μL min^{-1} (nano-ESI), and 5 μL min^{-1} (ESI). Nitrogen gas (99.995% purity) flow rates used in the ESI source include a sheath gas of 10−12 units and an auxiliary gas of 0−1 units. For nano-DESI, half of the PTFE filter (1/2 × 47 mm, Whatman) of each sample was taped to a glass slide. A stable solvent droplet (1:1; acetonitrile/water) was formed at a juncture between the solvent capillary and spraying capillary. The substrate containing the SOA sample was brought in contact with the droplet using micromanipulators, and the droplet was dragged over the sample while acquiring mass spectra for approximately 2−3 min. In addition to the samples, a solvent blank consisting of a clean substrate was analyzed following the same procedure in both positive and negative modes.

For nano-ESI and regular ESI, the remaining filter halves were solvent-extracted with 2 mL of a 1:1 mixture of acetonitrile and water under sonication for 15 min. The extracted solution was then passed through a 0.45 μm, PTFE membrane syringe filter (Fisherbrand) to remove any undissolved material. An additional 1 mL of solvent was passed through the PTFE membrane filter and collected with the filtered extracts to limit the loss of extracts on the filter surface. Data were acquired for approximately 2 min for nano-ESI and ESI. A solvent blank (a clean filter treated the same way as described above) was also analyzed for nano-ESI and ESI in the positive and negative mode.

The analysis procedure of the mass spectrometry data has been described previously.[89] Xcalibur was used to integrate portions of the scan and save the mass spectra as raw files. Then, the Decon2LS software program (https://omics.pnl.gov/software/decontools-decon2ls) was used to extract peak positions and intensities. Only peaks below m/z 700 were considered in analysis because peaks at larger m/z values had negligibly small abundances. Peaks that were present in the solvent blank with a solvent/sample peak abundance ratio in an excess of 0.1 were considered impurities and excluded from further analysis. All positive ions were assigned to formulas $C_{1-40}H_{2-80}O_{0-35}N_{0-3}Na_{0-1}^+$ with a m/z accuracy of 0.001. Protonation was the most common ionization mechanism in the positive ion mode, although a small fraction of the ions were monosodium adducts. Sodium adducts can form during direct infusion electrospray ionization in the positive mode.[90,91] All negative ions were assigned to formulas $C_{1-40}H_{2-80}O_{0-35}N_{0-3}^-$ assuming that deprotonation was the only ionization mechanism. Only closed-shell ions were permitted, and the elemental ratios were constrained to be 0.30 < H/C < 2.25 and 0.00 < O/C < 2.30 to ensure that elemental formula assignments were physically reasonable. Peaks that could not be assigned with the abovementioned constraints were assigned manually using the MIDAS molecular calculator (https://nationalmaglab.org/user-facilities/icr/icr-software). The ^{13}C isotope and other obvious impurities, signified by unreasonably high mass defects, were examined and removed from the final dataset. The N-containing species made up a small portion (<1%) of the total signal and were therefore treated as impurities and excluded. The formulas of the assigned ions were converted to the neutral formulas by removing Na^+, H^+, or NH_4^+, depending on the ionization mechanism in the positive mode and adding a H in the case of the negative mode. The assignments are reported in neutral mass of each species. The datasets for the positive and negative modes were aligned based on neutral mass and each mode was normalized so the sum of the intensities over all masses in a single mode would add up to one. Then the intensities were averaged between the modes for each mass for the combined dataset. All the peaks in the combined dataset were used to predict the viscosity.

2.4. Predictions of the Viscosity of SOA from Measurements of the Chemical Composition of the SOA. To predict viscosity of the SOA from the mass spectra, we followed the approach of DeRieux et al.[55] First, the glass transition temperature (T_g) of compound i was predicted from the mass spectra using the following equation:[55]

https://dx.doi.org/10.1021/acsearthspacechem.0c00296
ACS Earth Space Chem. 2021, 5, 305−318

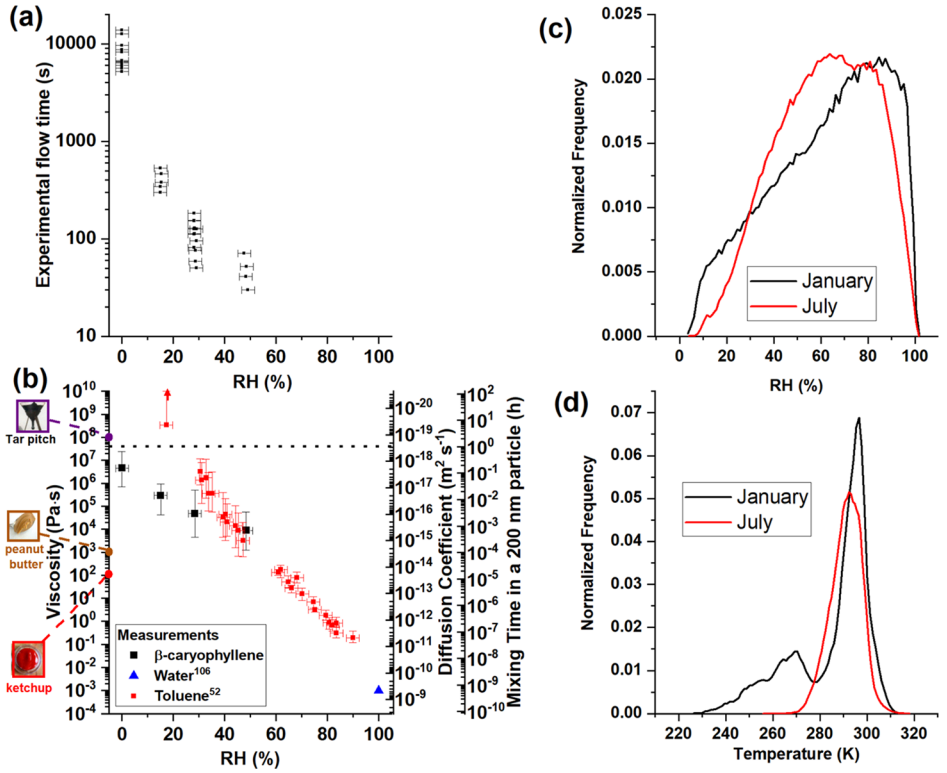

Figure 4. Panel (a) shows the experimental flow time, $\tau_{exp,flow}$, for poked particles as a function of RH. Panel (b) shows measured viscosities and calculated diffusion coefficients and mixing times of organic molecules in a 200 nm particle. The *x*-error bars correspond to uncertainties in the RH measurements and in panel (b), the *y*-error bars represent the upper and lower limits of the measured viscosities at each RH. The dotted line corresponds to a mixing time of 1 h. Also included in panel (b) are literature viscosity values for toluene SOA.[52] Pictures of common substances have been added to panel (b) as points of reference per Koop et al. (2011). The tar pitch image is from the tar pitch experiment (image courtesy of Wikimedia Commons, GNU Free Documentation License, University of Queensland, John Mainstone). Panels (c,d) show the RH and temperature frequency distributions in January (black line) and July (red line) in the global planetary boundary layer (i.e., the planetary boundary layer in both the northern and southern hemisphere) based on GEOS-Chem. RH and temperature conditions were only included if the monthly averaged concentration of organic aerosol were greater than 0.5 μg m^{-3} at the surface based on the output of GEOS-Chem.[46] Conditions where the organic aerosol concentrations were <0.5 μg m^{-3} were excluded, as aerosols at low concentrations are expected to be of less importance to climate or visibility.

$$T_{g,i} = (n_C^0 - \ln(n_C))b_C + \ln(n_H)b_H + \ln(n_C)\ln(n_H)b_{CH} + \ln(n_O)b_O + \ln(n_C)\ln(n_O)b_{CO} \quad (1)$$

where n_C, n_H, and n_O are the number of carbon, hydrogen, and oxygen atoms, respectively, of compound *i*. Values of the coefficients [n_C^0, b_C, b_H, b_{CH}, b_O, and b_{CO}] were [1.96, 61.99, −113.33, 28.74, 0, and 0] for CH compounds and [12.13, 10.95, −41.82, 21.61, 118.96, and −24.38] for CHO compounds.

Next, the T_g of the SOA under dry conditions ($T_{g,org}$) was estimated using the Gordon−Taylor equation assuming a Gordon−Taylor constant (k_{GT}) of 1:[70]

$$T_{g,org} = \sum_i w_i T_{g,i} \quad (2)$$

where w_i is the mass fraction of compound *i*. Following DeRieux et al.,[55] we assumed that w_i values were proportional to the relative abundances in the combined mass spectra dataset, I_i (eq 3), which is a known limitation of this approach:[55,92]

$$w_i = I_i \quad (3)$$

T_g of organic−water mixtures ($T_{g,mix}$) was then calculated using the Gordon−Taylor equation with a k_{GT} of 2.5:[70,93]

$$T_{g,mix} = \frac{(1 - w_{org})T_{g,H_2O} + w_{org}T_{g,org}\frac{1}{k_{GT}}}{(1 - w_{org}) + w_{org}\frac{1}{k_{GT}}} \quad (4)$$

where w_{org} is the mass fraction of the SOA and T_{g,H_2O} is the glass transition temperature of water (136 K).[94] The value of w_{org} can be calculated based on the mass concentration of water (m_{H_2O}) and the organics (m_{org}):

$$w_{org} = \frac{m_{org}}{m_{org} + m_{H_2O}} \quad (5)$$

Under humid conditions, m_{H_2O} was estimated using the effective hygroscopicity parameter (κ) and eq 6:[95]

$$m_{H_2O} = \frac{\kappa\rho_w m_{org}}{\rho_{org}\left(\frac{1}{a_w} - 1\right)} \quad (6)$$

where ρ_w and ρ_{org} are the densities of water and the SOA and a_w is the water activity, which corresponds to RH/100. The density of the SOA particles was assumed to be 990 kg m^{-3}[77] and the hygroscopicity parameter was assumed to be 0.04−0.001.[96,97]

Viscosity as a function of temperature (T) was then calculated from $T_{g,mix}$ using the Vogel−Tammann−Fulcher (VTF) equation:[55]

https://dx.doi.org/10.1021/acsearthspacechem.0c00296
ACS Earth Space Chem. 2021, 5, 305−318

$$\eta = \eta_{\infty} e^{T_0 D_f / T - T_0} \quad (7)$$

where D_f represents the fragility parameter and η_{∞} represents the viscosity at infinite temperature assumed to be 10^{-5} Pa s.[98,99] T_0 is the Vogel temperature calculated as $T_0 = \frac{39.17 T_{g,mix}}{D_f + 39.17}$, which is deduced from an assumed viscosity of 10^{12} Pa s at the glass transition temperature.[99] D_f, which characterizes the deviation of the temperature dependence of viscosity from an Arrhenius behavior,[98,100] was assumed to be 10 based on our previous study.[55] The value of D_f is assumed to be independent of RH.[54,55,101,102] This assumption is consistent with previous studies that found that the value of D_f in sucrose and citric acid is independent of water content, except for anhydrous sucrose.[99,103,104]

2.5. Prediction of Viscosity Using a Mole-Fraction Based Arrhenius Mixing Rule. The viscosities of SOA as a function of RH can also be estimated using the measured viscosities of pure water and dry SOA and mixing rules. In the following, we test a mole-fraction based Arrhenius mixing rule for predicting the viscosity of β-caryophyllene SOA as a function of RH. This mixing rule is expressed for our system using the following equation:[105]

$$\ln(\eta_{org,wet}) = x_{org} \ln(\eta_{org,dry}) + x_{H_2O} \ln(\eta_{H_2O}) \quad (8)$$

where $\eta_{org,wet}$ is the viscosity of the SOA and water mixture, $\eta_{org,dry}$ is the viscosity of the dry SOA, η_{H_2O} is the viscosity of pure water, x_{org} is the mole fraction of SOA in the SOA–water mixture, and x_{H_2O} is the mole fraction of water in the SOA–water mixture. For the viscosity of the dry SOA, we used 4.6×10^6 Pa s (which is based on our experimental data), and for the viscosity of pure water, we used 10^{-3} Pa s.[106] The mole fractions of SOA and water were calculated from the weight fractions of SOA and water using eq 9:

$$x_{SOA} = \frac{\frac{w_{org}}{M_{org}}}{\frac{w_{org}}{M_{org}} + \frac{w_{H_2O}}{M_{H_2O}}} \quad (9)$$

where w_{org} and w_{H_2O} are the weight fractions of the SOA and water, respectively, and M_{org} and M_{H_2O} are the molecular weights of the SOA and water, respectively. For the average molecular weight of the SOA, we used 271.0 g mol^{-1} based on the mass spectra and eq 14 (see below). The weight fraction of the SOA and water was estimated from the water activity using eq 5 and 6, an SOA density of 990 kg m^{-3},[77] and CCN-derived kappa values of 0.04–0.001 for SOA generated from the ozonolysis of β-caryophyllene in the presence of an OH scavenger.[96,97]

3. RESULTS AND DISCUSSION

3.1. Viscosity as a Function of RH. Values of $\tau_{exp,flow}$ as a function of RH were determined from each of the poke-flow measurements (Figure 4a). The $\tau_{exp,flow}$ values increased from ~48 s at 48% RH to ~2.5 h at 0% RH. Using the $\tau_{exp,flow}$ values and the particle dimensions, upper and lower limits for the viscosities were determined from fluid-flow simulations (Figure 4b). At an RH of 0%, the viscosity was between 6.9×10^5 and 2.4×10^7 Pa s and at an RH of 48%, the viscosity was between 1.3×10^3 and 5.6×10^4 Pa s. Some other types of SOA previously investigated with the poke-flow technique were more sensitive to RH over the same RH range. For example, the viscosity of SOA generated by the photo-oxidation of toluene is >10^8 Pa s at 17% RH but ~10^3 to 10^4 Pa s at ~50% RH (Figure 4b).[52] The weaker dependence on RH in the current experiments compared to toluene SOA is most likely because β-caryophyllene SOA has a lower hygroscopicity (κ = 0.04–0.001)[96,97] than toluene SOA (κ = 0.1–0.25).[107] Water acts as a plasticizer for SOA (i.e., as water content increases, viscosity decreases)[70] and the smaller hygroscopicity of β-caryophyllene SOA likely translates into a weaker dependence of viscosity on RH over the range of RH values investigated.

A few previous studies investigated particle rebound as a function of RH for SOA from sesquiterpenes.[37,108] The rebound studies were used to infer whether the SOA was in a liquid (viscosity $\lesssim 10^2$ Pa s) or a nonliquid state (viscosity $\gtrsim 10^2$ Pa s). Li et al.[37] inferred that the nonliquid-to-liquid transition occurred at an RH > 90% for SOA generated by the photo-oxidation of β-caryophyllene. Pajunoja et al.[108] inferred that the transition occurred at an RH of 70–90% for SOA from longifolene photo-oxidation, with an O/C-dependent transition RH. These studies are consistent with the current results.

3.2. Diffusion Coefficients and Mixing Times of Organic Molecules within β-Caryophyllene SOA as a Function of RH. Diffusion coefficients of organic molecules within SOA can be calculated from viscosity measurements using the Stokes–Einstein equation[43,48] or the fractional Stokes–Einstein equation.[43,44,48] A recent study showed that diffusion coefficients predicted with the Stokes–Einstein equation were in reasonable agreement with measured diffusion coefficients in most cases when the radius of the diffusing molecules (R_{diff}) was greater than or equal to the radius of the matrix molecules (R_{matrix}) and when the viscosities were between 10^{-3} and 10^6 Pa s.[44] A more recent study showed that the fractional Stokes–Einstein equation was able to predict 98% of observed diffusion coefficients roughly within the uncertainty of the measurement for R_{diff}/R_{matrix} values ranging from 0.31 to 1.75 and viscosities ranging from 10^{-3} to 10^{10} Pa s. Based on these findings, we used the fractional Stokes–Einstein equation to predict diffusions of organic molecules within the SOA:[109]

$$D = D_0 \times \left(\frac{\eta_0}{\eta}\right)^{\xi} \quad (10)$$

where ξ is the fractional exponent, η is the viscosity, η_0 is the viscosity of pure water (10^{-3} Pa s at a temperature of 293 K), and D_0 is the diffusion coefficient in pure water, calculated using the Stokes–Einstein equation:

$$D_0 = \frac{kT}{6\pi\eta_0 R_{diff}} \quad (11)$$

where k is the Boltzmann constant, T is the temperature, and R_{diff} is the radius of the diffusing molecule. We assumed a radius of 0.47 nm for the diffusing molecule, based on a molecular weight of 254 g mol^{-1} for some common first-generation β-caryophyllene ozonolysis products,[110] a density of 990 kg m^{-3},[77] and an assumed spherical geometry of the diffusing molecule. The value of ξ was calculated using eq 12:[44]

$$\xi = 1 - \left[A \exp\left(-B \frac{R_{diff}}{R_{matrix}}\right)\right] \quad (12)$$

where A corresponds to 0.73 and B corresponds to 1.79.[44] A value of 1 was assumed for R_{diff}/R_{matrix}. Based on the fractional Stokes–Einstein equation, the diffusion coefficients ranged from ~4.1×10^{-16} m^2 s^{-1} at 48% RH to ~1.8×10^{-18} m^2 s^{-1} at 0% RH

https://dx.doi.org/10.1021/acsearthspacechem.0c00296
ACS Earth Space Chem. 2021, 5, 305–318

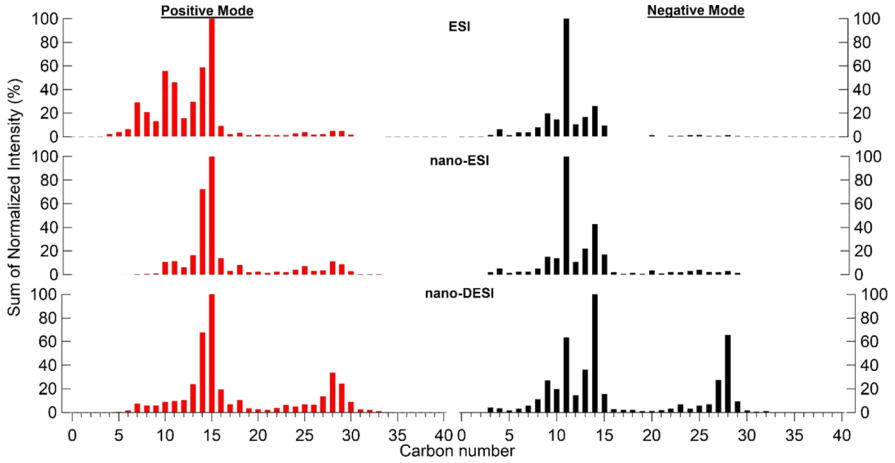

Figure 5. Sum of intensities of all molecular formula assignments based on carbon number for three ionization techniques (ESI, nano-ESI, and nano-DESI), which are normalized to the maximum intensity peak in each respective spectrum.

(Figure 4b, secondary *Y*-axis). The diffusion coefficients calculated using the fractional Stokes−Einstein equation correspond to bulk diffusion coefficients. These diffusion coefficients should be applicable to atmospheric particles that have diameters greater than ∼0.1 μm,[19,111] which covers the majority of the mass of atmospheric particles. However, the diffusion coefficients may not apply to particles with diameters <0.1 μm as surface and confinement effects may become important for these particle diameters.[111−113]

Diffusion coefficients were converted into characteristic mixing timescales of organic molecules within 200 nm SOA particles using eq 13:[12]

$$\tau_{mix} = \frac{{d_p}^2}{4\pi^2 D} \quad (13)$$

where τ_{mix} is the mixing time of the particle, d_p is the diameter of the particle, and D is the diffusion coefficient of the diffusing molecule, calculated using eq 10. The mixing time corresponds to the time it takes for the concentration of the diffusing molecules at the center of the SOA particle to differ from the equilibrium concentration by less than $1/e$ for nonreactive partitioning. The SOA particle was assumed to have a diameter of 200 nm, which is within the range of SOA particle sizes found in the atmosphere.[114−116] The calculated mixing times ranged from ∼0.2 h at 0% RH to <3 s at 48% RH (Figure 4b, secondary *Y*-axis).

Chemical transport models typically assume that the mixing times within SOA are less than ∼1 h.[1] Based on our results, the mixing time within a 200 nm β-caryophyllene SOA is <1 h at all RHs when the temperature is 292−294 K (Figure 4b). Based on previous calculations, the RH in the planetary boundary layer is nearly always ≥10% RH when the organic aerosol concentrations are >0.5 μg m^{-3} at the surface (Figure 4c).[117] Furthermore, the temperature in the planetary boundary layer is most often 280−290 K when the organic aerosol concentrations are >0.5 μg m^{-3} at the surface (Figure 4d).[117] Hence, the mixing times within β-caryophyllene SOA are <1 h for a large majority of RH and temperature conditions in the planetary boundary layer when the organic aerosol concentrations are >0.5 μg m^{-3} at the surface. Conditions where the organic aerosol concentrations were <0.5 μg m^{-3} were excluded, as aerosols at low concentrations are expected to be of less importance to climate or visibility.

One caveat to the discussion above is that the mass concentration of the SOA generated in the environmental chamber was 50−60 μg m^{-3}, which is higher than typical mass concentrations of biogenic SOA in the atmosphere.[3,118] Previous studies have shown that for some types of SOA, the viscosity, and hence mixing times, increases with a decrease in mass concentration of SOA in the reactor.[69,80,119] Reducing the SOA mass concentration removes compounds with higher vapor pressures from the particles.[120] These higher vapor pressure compounds have lower glass transition temperatures.[54,55] Additional studies are needed to determine the effect of SOA mass concentration on the viscosity of β-caryophyllene SOA.

Related to the mixing times shown in Figure 4b, Ye et al.[121] investigated the mixing of semivolatile vapors from α-pinene SOA and toluene SOA within β-caryophyllene SOA (formed by ozonolysis, as in the current experiments). In these experiments, β-caryophyllene SOA took up only a small amount of semivolatile vapors (≤10% change in β-caryophyllene SOA mass) over a period of 2 h at 50% RH. The authors suggested two possible explanations for the limited uptake of the semivolatile vapors: (1) diffusion-limited uptake and (2) immiscibility (e.g., nonideality) of semivolatile vapors from α-pinene SOA and toluene SOA within β-caryophyllene SOA.[121] The size of SOA particles studied by Ye et al.[121] ranged from 200 to 700 nm in diameter. Using the method discussed above, we calculated the mixing times of organic molecules within 450 nm β-caryophyllene SOA particles as a function of RH (Figure S6). Based on these calculations, the mixing times of organic molecules within a 450 nm β-caryophyllene SOA particle at 48% RH are 2.3−62 s. These calculations suggested that the limited uptake of semivolatile vapors from α-pinene SOA and toluene SOA within β-caryophyllene SOA observed by Ye et al.[121] was due to immiscibility rather than diffusion-limited uptake. However, Ye et al.[121] used SOA generated with mass concentrations of 3.4−6.4 μg m^{-3} compared to the mass loading of 50−60 μg m^{-3} used in this study. Since viscosity can increase with a decrease in SOA mass concentration, the SOA studied by Ye et al.[121] may have been more viscous than the SOA in the current study, leading to longer mixing times than calculated from our data.

3.3. Chemical Composition of the SOA Based on Mass Spectrometry. The full mass spectra are shown in Figure S7, and relative peak abundances from the mass spectra are shown in Figure 5 as a function of carbon number. β-Caryophyllene

https://dx.doi.org/10.1021/acsearthspacechem.0c00296
ACS Earth Space Chem. 2021, 5, 305−318

($C_{15}H_{24}$) is expected to produce mainly C14−C15 compounds during ozonolysis, but smaller compounds resulting from more extensive backbone fragmentation and larger compounds resulting from oligomerization are also possible. We observed that ESI and nano-ESI favored the detection of smaller compounds compared to the nano-DESI. This effect is especially noticeable in the positive ion-mode ESI data, manifesting itself in unexpectedly high peak abundances in C5−C10 compounds. In the negative ion-mode spectra, the peak abundance is also shifted from the expected C14−C15 compounds in nano-DESI to smaller compounds in ESI and nano-ESI. Even though instrument conditions were optimized for each method, it is possible that fewer compounds experienced in-source fragmentation in nano-DESI than in other ionization modes. The ionization mechanism for nano-DESI has been shown to be better-suited for the detection of chemically labile compounds compared to ESI.[122,123] It has previously been found that chemically labile compounds may dissociate in solution during ESI-based analysis. Due to the shorter residence time of the sample in the solvent during nano-DESI, this dissociation is minimized.[122] Therefore, for the remainder of the document, we will focus on the nano-DESI results, which provide information on a broader range of SOA compounds.

Shown in Figure 6 are nano-DESI mass spectra, with the five most abundant peaks in the positive and negative mode

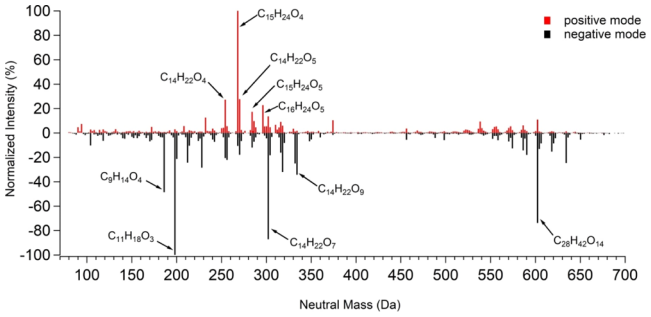

Figure 6. Nano-DESI mass spectrum taken in the positive mode (red spectrum) and negative mode (black spectrum). The signals were normalized to the highest intensity in each respective mode. The five most abundant peaks in each mode are labeled by the corresponding neutral (unionized) molecular formulas.

identified. Approximately 1000 peaks were observed in the positive mode compared to 700 peaks observed in the negative mode. β-Caryophyllene has two double bonds (Figure 1) and attack by ozone on the more-reactive endocyclic double bond will generally lead to ring-opening products retaining the C15 carbon number. Attack on the less-reactive exocyclic double bond generally leads to C14 products. Indeed, the most-abundant peaks in the positive ion-mode mass spectra were C14 and C15 species. It is common to observe $C_{15}H_{24}O_n$ products in mass spectra of oxidized sesquiterpenes.[124,125] The major C15 products identified include $C_{15}H_{24}O_4$ and $C_{15}H_{24}O_5$, which have been reported as first-generation ozonolysis products.[110,126] Some of the major C14 products identified include $C_{14}H_{22}O_4$, $C_{14}H_{22}O_5$, and $C_{14}H_{22}O_7$, which have been reported as second-generation ozonolysis products.[110,126] The $C_{14}H_{22}O_9$ product was previously reported in Richters et al.[127] as a highly oxidized reaction product of β-caryophyllene ozonolysis formed via an extended autoxidation pathway.

In addition to C14 and C15 species, other carbon numbers were also observed, which result from fragmentation of Criegee intermediates during ozonolysis, other radical-driven secondary chemistry, and oligomerization processes occurring in the gas and particle phase. The C11 product $C_{11}H_{18}O_3$ has been reported as a second-generation ozonolysis product of β-caryophyllene.[110,126] The C28 peak $C_{28}H_{42}O_{14}$ has more carbon atoms than β-caryophyllene, indicating the formation of oligomers from β-caryophyllene oxidation products. Some other major peaks include $C_9H_{14}O_4$ and $C_{16}H_{24}O_5$, which have not been reported previously and are likely second- or third-generation ozonolysis products of β-caryophyllene. These two compounds have O/C ratios of 0.44 and 0.31, respectively, which is consistent with O/C ratios of second-generation products.[110]

3.4. Viscosity Predictions Based on the Measured Chemical Composition. For viscosity predictions, we used the nano-DESI mass spectrometry results, since this method of ionization detected the widest spectrum of SOA compounds, based on Figure 5. As mentioned in Section 2.4, we assumed that the mass fraction of each compound was proportional to its relative peak abundance in the combined mass spectra dataset (eq 3).[55,92] We found that predictions based on this assumption and the nano-DESI results drastically overpredicted the viscosity (Figure 7a). For example, under dry conditions, the predicted viscosities were up to 6 orders of magnitude larger than the measured viscosities.

ESI-based methods are known to be more sensitive to larger, oligomeric compounds,[128,129] and this may be the reason, at least in part, for the discrepancy between the measured viscosity

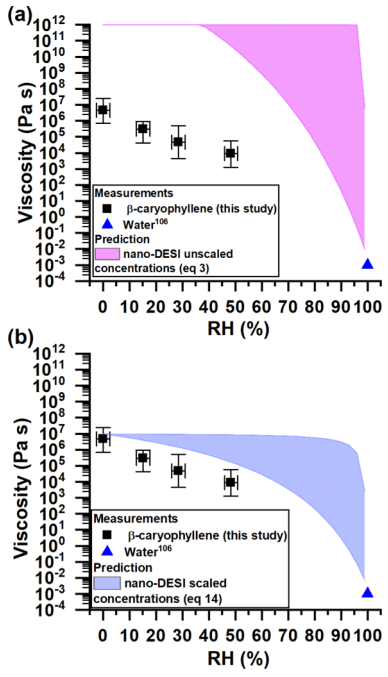

Figure 7. Comparison of measured and predicted viscosities as a function of RH. The x-error bars correspond to uncertainties in the RH measurements, and the y-error bars correspond to the upper and lower limits of viscosity at each RH. Panel (a) shows the viscosity predictions using the averaged positive- and negative-ion mode mass spectrometry data where it was assumed that the weight fraction of the individual SOA species was proportional to the mass spectrum signal intensities (eq 3). Panel (b) shows the viscosity predictions using the averaged mass spectrometry data assuming a relation between weight fraction and intensity given in eq 14.

https://dx.doi.org/10.1021/acsearthspacechem.0c00296
ACS Earth Space Chem. 2021, 5, 305−318

and predicted viscosity. To investigate if this may be important to our studies, as a second step in our analysis, we used the adjusted mass approach based on the work of Nguyen et al.[129] to predict the mass fraction of each compound in the SOA:

$$w_i = \frac{I_i}{H/C_i \times M_i} \quad (14)$$

where M_i is the molecular weight of the compound, H/C_i is the hydrogen-to-carbon ratio of the compound, and $H/C_i \times M_i$ is the adjusted mass. This scaling was used to approximately account for the impact of molecular weight and degree of unsaturation (represented by the H/C ratio) on the ionization efficiency of the individual compounds. This is the same relation developed by Nguyen et al.[129] based on the addition of calibration standards to a realistic SOA matrix, except Nguyen et al.[129] included a term to account for the limit of detection (LOD) of the compounds, which was found to inversely correlate with molecular weight and found to be small for compounds when the adjusted mass was >200 Da. In the absence of better information, we neglected the LOD term as more than 90% of the compounds detected via mass spectrometry have an adjusted mass >200 Da.

The viscosities predicted using eq 14 better overlapped with the measured viscosities (Figure 7b). It is especially remarkable that the predicted viscosity matches with the measured viscosity at 0% RH, indicating that the T_g parameterization and prediction method (eqs 1 and 2) work well. While ESI-based methods selectively ionize only oxidized species, the agreement implies that nano-DESI is capable of detecting the majority of the compounds present in β-caryophyllene SOA that contribute to its viscosity. It also suggests that the poor agreement between the measured viscosities and our initial predictions (assuming linearity between w_i and I_i) may be, in part, due to the enhanced sensitivity of ESI methods to larger molecular weight compounds. At RH values of 15−48%, the predicted viscosities using eq 14 are still larger than the measured viscosities, although the differences are much smaller than in Figure 7a. These differences may be due to uncertainties in the parameters or assumptions used to generate the predictions. Interestingly, in our previous studies using toluene SOA and diesel fuel SOA, we observed reasonable agreement between measured viscosities and predictions when we assumed a linear relation (i.e., eq 3).[55,92] To investigate this further, we have redone these comparisons using eqs 3 and 14. The results show that using the relation in eq 14 results in similar or improved predictions of the viscosity compared to eq 3 for both the toluene SOA and diesel fuel SOA (Figures S8 and S9), consistent with the trend observed for β-caryophyllene SOA (although the difference in the predicted results is not nearly as dramatic as for β-caryophyllene SOA).

The ultimate dataset for viscosity predictions would be a full roster of the actual (rather than estimated) mass fractions of all SOA compounds. Because of the overwhelmingly large number of SOA compounds and lack of appropriate calibration standards, no existing experimental method can provide such a dataset. However, our analysis suggests that an approximate estimation of mass fractions based on eq 14 can work reasonably well for the purposes of predicting material viscosity. Specifically, we have shown that nano-DESI can be used with eqs 1, 2, and 4−7 and the relation between w_i and I_i shown in eq 14 to provide an improved prediction of viscosity for toluene SOA, diesel fuel SOA, and β-caryophyllene SOA compared to using the assumption in eq 3.

3.5. Viscosity Predictions Based on Mole-Fraction Based Arrhenius Mixing Rule. The viscosities of SOA as a function of RH were also estimated using a mole-fraction based Arrhenius mixing rule (eq 8) and the measured viscosities of pure water and dry SOA. For a viscosity of the dry SOA, we used 4.6×10^6 Pa s (which is consistent with our experimental data) and for the viscosity of pure water, we used 10^{-3} Pa s.[106]

The predictions based on this approach overlapped with the measured viscosities (Figure 8). This is consistent with the recent studies by Gervasi et al.,[56] who showed that a mole-fraction based mixing rule is the best choice among simple mixing rules for predicting viscosity in binary aqueous systems. These predicted viscosities had large uncertainties for RH values ranging from approximately 30 to 95%, mainly due to the large uncertainty in the κ values used to predict the mole fraction of water in the SOA. The predictions based on the chemical composition and the method from DeRieux et al.[55] (Figure 7) also had large uncertainties at similar RH values for the same reason. This highlights that accurate and precise measurements of κ values for SOA are needed for predicting viscosities of SOA as a function of RH.

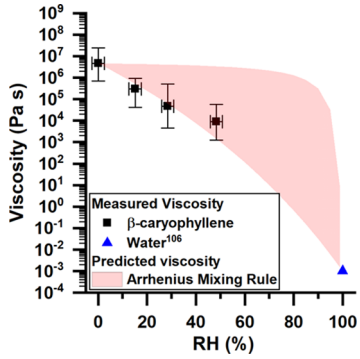

Figure 8. Measured viscosities and predicted viscosities using a mole-fraction based Arrhenius mixing rule. For the measurements, the x-error bars correspond to uncertainties in the RH and the y-error bars represent the upper and lower limits of the simulated viscosities at each RH. The uncertainties in the predictions are due to uncertainties in the hygroscopicity of the SOA. For the hygroscopicity, we used a range of CCN-derived kappa values of 0.04−0.001.[96,97]

4. SUMMARY AND CONCLUSIONS

Viscosity was measured as a function of RH for SOA generated via the ozonolysis of β-caryophyllene. The viscosity was 1.3×10^3 to 5.6×10^4 Pa s at 48% RH, and it increased to 6.9×10^5 to 2.4×10^7 Pa s at 0% RH, where the ranges correspond to measurement and data analysis uncertainties. Diffusion coefficients were calculated from the viscosities using the fractional Stokes−Einstein equation and ranged from $\sim 4.1 \times 10^{-16}$ m^2 s^{-1} at 48% RH to $\sim 1.8 \times 10^{-18}$ m^2 s^{-1} at 0% RH. Mixing times of organic molecules within 200 nm SOA particles were calculated from the diffusion coefficients and ranged from <3 s at 48% RH to 0.2 h at 0% RH. Based on these values, mixing times within 200 nm β-caryophyllene SOA are fast (<1 h) for RH and temperatures typically found in the planetary boundary layer.

The chemical composition of the SOA was determined with nano-DESI mass spectrometry. The most-abundant peaks in the

https://dx.doi.org/10.1021/acsearthspacechem.0c00296
ACS Earth Space Chem. 2021, 5, 305−318

mass spectra were C15 and C14 peaks, corresponding to the first- and second-generation ozonolysis products. Another abundant peak in the mass spectra was a C28 peak, likely the result of dimerization of the β-caryophyllene oxidation products. We note that ESI and nano-ESI favored the detection of smaller compounds compared to nano-DESI, and the fact that relative peak abundances from the three ionization methods do not fully agree with each other highlights the difficulty of estimating relative abundances of SOA compounds using direct infusion methods. In this study, we assumed that nano-DESI provides the most accurate information about SOA composition because it is known to better detect labile compounds.

The viscosity data and the chemical composition from mass spectrometry were used to test the accuracy of the method from DeRieux et al.[55] for predicting the viscosity of β-caryophyllene SOA. Using raw peak nano-DESI abundances in the mass spectra as substitutes of mass fractions led to a drastic overprediction of the viscosity by up to 6 orders of magnitude (depending on the RH). However, when the peak abundances were adjusted to account for the sensitivity of the electrospray ionization to larger molecular weight components using an empirical relationship suggested by Nguyen et al.,[129] the predicted viscosities better overlapped with the measured viscosities. Furthermore, the same method produced better or similar predictions for our previous observations of viscosity of toluene SOA and diesel fuel SOA. These results further highlight the level of sensitivity of viscosity predictions to the method used for relating peak abundances to relative concentrations in direct infusion mass spectra.

We also tested the accuracy of a mole-fraction based Arrhenius mixing rule for predicting viscosity as a function of RH from the viscosity of water and the dry SOA. For this case, the predictions overlapped with the measured data.

■ ASSOCIATED CONTENT

Supporting Information

The Supporting Information is available free of charge at https://pubs.acs.org/doi/10.1021/acsearthspacechem.0c00296.

OH scavenger efficiency calculations; mixing time of water in experiment calculations; water mixing times used in experiments; parameters used for fluid simulations; schematic of the environmental chamber; chamber residence time experimental results; schematic of poke-flow setup; viscosities as a function of conditioning time; geometry of the model used to simulate viscosity; mixing time in 450 nm SOA; mass spectra of all ionization modes; viscosity predictions for toluene SOA; and viscosity predictions for diesel fuel SOA (PDF)

■ AUTHOR INFORMATION

Corresponding Authors

Sergey A. Nizkorodov − *Department of Chemistry, University of California, Irvine, California 92697-2025, United States;* orcid.org/0000-0003-0891-0052; Email: nizkorod@uci.edu

Allan K. Bertram − *Department of Chemistry, University of British Columbia, Vancouver, British Columbia V6T 1Z1, Canada;* orcid.org/0000-0002-5621-2323; Email: bertram@chem.ubc.ca

Authors

Adrian M. Maclean − *Department of Chemistry, University of British Columbia, Vancouver, British Columbia V6T 1Z1, Canada;* orcid.org/0000-0003-0901-5287

Natalie R. Smith − *Department of Chemistry, University of California, Irvine, California 92697-2025, United States*

Ying Li − *Department of Chemistry, University of California, Irvine, California 92697-2025, United States*

Yuanzhou Huang − *Department of Chemistry, University of British Columbia, Vancouver, British Columbia V6T 1Z1, Canada*

Anusha P. S. Hettiyadura − *Department of Chemistry, Purdue University, West Lafayette, Indiana 47907, United States;* orcid.org/0000-0002-5757-9784

Giuseppe V. Crescenzo − *Department of Chemistry, University of British Columbia, Vancouver, British Columbia V6T 1Z1, Canada*

Manabu Shiraiwa − *Department of Chemistry, University of California, Irvine, California 92697-2025, United States;* orcid.org/0000-0003-2532-5373

Alexander Laskin − *Department of Chemistry, Purdue University, West Lafayette, Indiana 47907, United States;* orcid.org/0000-0002-7836-8417

Complete contact information is available at: https://pubs.acs.org/10.1021/acsearthspacechem.0c00296

Notes

The authors declare no competing financial interest.

■ ACKNOWLEDGMENTS

The UBC team was funded by the Natural Science and Engineering Research Council of Canada. The UCI team acknowledges support from grant DE-SC0018349 from the US Department of Energy (DOE). M.S. also acknowledges funding from the National Science Foundation (AGS-1654104). The PU team acknowledges additional support from discretional PU start-up funds allocated to A.L. N.R.S. thanks the University of California, Irvine Department of Chemistry, for support with Rowland Graduate Research Fellowship.

■ REFERENCES

(1) Hallquist, M.; Wenger, J. C.; Baltensperger, U.; Rudich, Y.; Simpson, D.; Claeys, M.; Dommen, J.; Donahue, N. M.; George, C.; Goldstein, A. H.; Hamilton, J. F.; Herrmann, H.; Hoffmann, T.; Iinuma, Y.; Jang, M.; Jenkin, M. E.; Jimenez, J. L.; Kiendler-Scharr, A.; Maenhaut, W.; McFiggans, G.; Mentel, T. F.; Monod, A.; Prévôt, A. S. H.; Seinfeld, J. H.; Surratt, J. D.; Szmigielski, R.; Wildt, J. The Formation, Properties and Impact of Secondary Organic Aerosol: Current and Emerging Issues. *Atmos. Chem. Phys.* **2009**, *9*, 5155−5236.

(2) Ervens, B.; Turpin, B. J.; Weber, R. J. Secondary Organic Aerosol Formation in Cloud Droplets and Aqueous Particles (AqSOA): A Review of Laboratory, Field and Model Studies. *Atmos. Chem. Phys.* **2011**, *11*, 11069−11102.

(3) Spracklen, D. V.; Jimenez, J. L.; Carslaw, K. S.; Worsnop, D. R.; Evans, M. J.; Mann, G. W.; Zhang, Q.; Canagaratna, M. R.; Allan, J.; Coe, H.; McFiggans, G.; Rap, A.; Forster, P. Aerosol Mass Spectrometer Constraint on the Global Secondary Organic Aerosol Budget. *Atmos. Chem. Phys.* **2011**, *11*, 12109−12136.

(4) Kanakidou, M.; Seinfeld, J. H.; Pandis, S. N.; Barnes, I.; Dentener, F. J.; Facchini, M. C.; Van Dingenen, R.; Ervens, B.; Nenes, A.; Nielsen, C. J.; Swietlicki, E.; Putaud, J. P.; Balkanski, Y.; Fuzzi, S.; Horth, J.; Moortgat, G. K.; Winterhalter, R.; Myhre, C. E. L.; Tsigaridis, K.; Vignati, E.; Stephanou, E. G.; Wilson, J. Organic Aerosol and Global Climate Modelling: A Review. *Atmos. Chem. Phys.* **2005**, *5*, 1053−1123.

(5) Khan, M. A. H.; Jenkin, M. E.; Foulds, A.; Derwent, R. G.; Percival, C. J.; Shallcross, D. E. A Modeling Study of Secondary Organic Aerosol Formation from Sesquiterpenes Using the STOCHEM Global Chemistry and Transport Model. *J. Geophys. Res.* **2017**, *122*, 4426−4439.
(6) Sakulyanontvittaya, T.; Guenther, A.; Helmig, D.; Milford, J.; Wiedinmyer, C. Secondary Organic Aerosol from Sesquiterpene and Monoterpene Emissions in the United States. *Environ. Sci. Technol.* **2008**, *42*, 8784−8790.
(7) Yee, L. D.; Isaacman-VanWertz, G.; Wernis, R. A.; Meng, M.; Rivera, V.; Kreisberg, N. M.; Hering, S. V.; Bering, M. S.; Glasius, M.; Upshur, M. A.; Gray Bé, A.; Thomson, R. J.; Geiger, F. M.; Offenberg, J. H.; Lewandowski, M.; Kourtchev, I.; Kalberer, M.; de Sá, S.; Martin, S. T.; Alexander, M. L.; Palm, B. B.; Hu, W.; Campuzano-Jost, P.; Day, D. A.; Jimenez, J. L.; Liu, Y.; McKinney, K. A.; Artaxo, P.; Viegas, J.; Manzi, A.; Oliveira, M. B.; de Souza, R.; Machado, L. A. T.; Longo, K.; Goldstein, A. H. Observations of Sesquiterpenes and Their Oxidation Products in Central Amazonia during the Wet and Dry Seasons. *Atmos. Chem. Phys.* **2018**, *18*, 10433−10457.
(8) Ying, Q.; Li, J.; Kota, S. H. Significant Contributions of Isoprene to Summertime Secondary Organic Aerosol in Eastern United States. *Environ. Sci. Technol.* **2015**, *49*, 7834−7842.
(9) Bouvier-Brown, N. C.; Goldstein, A. H.; Gilman, J. B.; Kuster, W. C.; de Gouw, J. A. In-situ ambient quantification of monoterpenes, sesquiterpenes, and related oxygenated compounds during BEARPEX 2007: implications for gas- and particle-phase chemistry. *Atmos. Chem. Phys.* **2009**, *9*, 5505−5518.
(10) Helmig, D.; Ortega, J.; Duhl, T.; Tanner, D.; Guenther, A.; Harley, P.; Wiedinmyer, C.; Milford, J.; Sakulyanontvittaya, T. Sesquiterpene Emissions from Pine Trees − Identifications, Emission Rates and Flux Estimates for the Contiguous United States. *Environ. Sci. Technol.* **2007**, *41*, 1545−1553.
(11) Guenther, A. B.; Jiang, X.; Heald, C. L.; Sakulyanontvittaya, T.; Duhl, T.; Emmons, L. K.; Wang, X. The Model of Emissions of Gases and Aerosols from Nature Version 2.1 (MEGAN2.1): An Extended and Updated Framework for Modeling Biogenic Emissions. *Geosci. Model Dev.* **2012**, *5*, 1471−1492.
(12) Seinfeld, J. H.; Pandis, S. N. *Atmospheric Chemistry and Physics*, 2nd ed.; John Wiley and Sons: Hoboken, NJ, 2006.
(13) *IPCC 2013: Climate Change 2013: The Physical Science Basis. Contribution of Working Group I to the Fifth Assessment Report of the Intergovernmental Panel on Climate Change*; Stocker, T. F., Quin, D., Plattner, G.-K., Tignor, M. M. B., Allen, S. K., Boschung, J., Nauels, A., Xia, Y., Bex, V., Midgley, P. M., Eds.; Cambridge Univ Press: Cambridge, U.K., 2013.
(14) Finlayson-Pitts, B. J.; Pitts, J. N. *Chemistry of the Upper and Lower Atmosphere*; Academic Press: San Diego, 2000.
(15) Knopf, D. A.; Alpert, P. A.; Wang, B. The Role of Organic Aerosol in Atmospheric Ice Nucleation: A Review. *ACS Earth Space Chem.* **2018**, *2*, 168−202.
(16) Pope, C. A., III; Dockery, D. W. Health Effects of Fine Particulate Air Pollution: Lines That Connect. *J. Air Waste Manage. Assoc.* **2006**, *56*, 709−742.
(17) Shiraiwa, M.; Ueda, K.; Pozzer, A.; Lammel, G.; Kampf, C. J.; Fushimi, A.; Enami, S.; Arangio, A. M.; Fröhlich-Nowoisky, J.; Fujitani, Y.; Furuyama, A.; Lakey, P. S. J.; Lelieveld, J.; Lucas, K.; Morino, Y.; Pöschl, U.; Takahama, S.; Takami, A.; Tong, H.; Weber, B.; Yoshino, A.; Sato, K. Aerosol Health Effects from Molecular to Global Scales. *Environ. Sci. Technol.* **2017**, *51*, 13545−13567.
(18) Lelieveld, J.; Evans, J. S.; Fnais, M.; Giannadaki, D.; Pozzer, A. The Contribution of Outdoor Air Pollution Sources to Premature Mortality on a Global Scale. *Nature* **2015**, *525*, 367−371.
(19) Shiraiwa, M.; Ammann, M.; Koop, T.; Pöschl, U. Gas Uptake and Chemical Aging of Semisolid Organic Aerosol Particles. *Proc. Natl. Acad. Sci. U.S.A.* **2011**, *108*, 11003−11008.
(20) Shiraiwa, M.; Seinfeld, J. H. Equilibration Timescale of Atmospheric Secondary Organic Aerosol Partitioning. *Geophys. Res. Lett.* **2012**, *39*. DOI: 10.1029/2012gl054008.
(21) Zaveri, R. A.; Easter, R. C.; Shilling, J. E.; Seinfeld, J. H. Modeling Kinetic Partitioning of Secondary Organic Aerosol and Size Distribution Dynamics: Representing Effects of Volatility, Phase State, and Particle-Phase Reaction. *Atmos. Chem. Phys.* **2014**, *14*, 5153−5181.
(22) Zaveri, R. A.; Shilling, J. E.; Zelenyuk, A.; Liu, J.; Bell, D. M.; D'Ambro, E. L.; Gaston, C. J.; Thornton, J. A.; Laskin, A.; Lin, P.; Wilson, J.; Easter, R. C.; Wang, J.; Bertram, A. K.; Martin, S. T.; Seinfeld, J. H.; Worsnop, D. R. Growth Kinetics and Size Distribution Dynamics of Viscous Secondary Organic Aerosol. *Environ. Sci. Technol.* **2018**, *52*, 1191−1199.
(23) Shiraiwa, M.; Yee, L. D.; Schilling, K. A.; Loza, C. L.; Craven, J. S.; Zuend, A.; Ziemann, P. J.; Seinfeld, J. H. Size Distribution Dynamics Reveal Particle-Phase Chemistry in Organic Aerosol Formation. *Proc. Natl. Acad. Sci. U.S.A.* **2013**, *110*, 11746−11750.
(24) Kim, Y.; Sartelet, K.; Couvidat, F. Modeling the Effect of Non-Ideality, Dynamic Mass Transfer and Viscosity on SOA Formation in a 3-D Air Quality Model. *Atmos. Chem. Phys.* **2019**, *19*, 1241−1261.
(25) Yli-Juuti, T.; Pajunoja, A.; Tikkanen, O. P.; Buchholz, A.; Faiola, C.; Väisänen, O.; Hao, L.; Kari, E.; Peräkylä, O.; Garmash, O.; Shiraiwa, M.; Ehn, M.; Lehtinen, K.; Virtanen, A. Factors controlling the evaporation of secondary organic aerosol from α-pinene ozonolysis. *Geophys. Res. Lett.* **2017**, *44*, 2562−2570.
(26) Zhang, Y.; Chen, Y.; Lei, Z.; Olson, N. E.; Riva, M.; Koss, A. R.; Zhang, Z.; Gold, A.; Jayne, J. T.; Worsnop, D. R.; Onasch, T. B.; Kroll, J. H.; Turpin, B. J.; Ault, A. P.; Surratt, J. D. Joint Impacts of Acidity and Viscosity on the Formation of Secondary Organic Aerosol from Isoprene Epoxydiols (IEPOX) in Phase Separated Particles. *ACS Earth Space Chem.* **2019**, *3*, 2646−2658.
(27) Zelenyuk, A.; Imre, D.; Beránek, J.; Abramson, E.; Wilson, J.; Shrivastava, M. Synergy between Secondary Organic Aerosols and Long-Range Transport of Polycyclic Aromatic Hydrocarbons. *Environ. Sci. Technol.* **2012**, *46*, 12459−12466.
(28) Keyte, I. J.; Harrison, R. M.; Lammel, G. Chemical reactivity and long-range transport potential of polycyclic aromatic hydrocarbons - a review. *Chem. Soc. Rev.* **2013**, *42*, 9333−9391.
(29) Mu, Q.; Shiraiwa, M.; Octaviani, M.; Ma, N.; Ding, A.; Su, H.; Lammel, G.; Pöschl, U.; Cheng, Y. Temperature Effect on Phase State and Reactivity Controls Atmospheric Multiphase Chemistry and Transport of PAHs. *Sci. Adv.* **2018**, *4* (). DOI: 10.1126/sciadv.aap7314.
(30) Shrivastava, M.; Lou, S.; Zelenyuk, A.; Easter, R. C.; Corley, R. A.; Thrall, B. D.; Rasch, P. J.; Fast, J. D.; Massey Simonich, S. L.; Shen, H.; Tao, S. Global Long-Range Transport and Lung Cancer Risk from Polycyclic Aromatic Hydrocarbons Shielded by Coatings of Organic Aerosol. *Proc. Natl. Acad. Sci. U.S.A.* **2017**, *114*, 1246−1251.
(31) Friedman, C. L.; Pierce, J. R.; Selin, N. E. Assessing the Influence of Secondary Organic versus Primary Carbonaceous Aerosols on Long-Range Atmospheric Polycyclic Aromatic Hydrocarbon Transport. *Environ. Sci. Technol.* **2014**, *48*, 3293−3302.
(32) Steimer, S. S.; Lampimäki, M.; Coz, E.; Grzinic, G.; Ammann, M. The Influence of Physical State on Shikimic Acid Ozonolysis: A Case for in Situ Microspectroscopy. *Atmos. Chem. Phys.* **2014**, *14*, 10761−10772.
(33) Houle, F. A.; Hinsberg, W. D.; Wilson, K. R. Oxidation of a Model Alkane Aerosol by OH Radical: The Emergent Nature of Reactive Uptake. *Phys. Chem. Chem. Phys.* **2015**, *17*, 4412−4423.
(34) Li, Z.; Smith, K. A.; Cappa, C. D. Influence of Relative Humidity on the Heterogeneous Oxidation of Secondary Organic Aerosol. *Atmos. Chem. Phys.* **2018**, *18*, 14585−14608.
(35) Hinks, M. L.; Brady, M. V.; Lignell, H.; Song, M.; Grayson, J. W.; Bertram, A. K.; Lin, P.; Laskin, A.; Laskin, J.; Nizkorodov, S. A. Effect of Viscosity on Photodegradation Rates in Complex Secondary Organic Aerosol Materials. *Phys. Chem. Chem. Phys.* **2016**, *18*, 8785−8793.
(36) Berkemeier, T.; Steimer, S. S.; Krieger, U. K.; Peter, T.; Pöschl, U.; Ammann, M.; Shiraiwa, M. Ozone Uptake on Glassy, Semi-Solid and Liquid Organic Matter and the Role of Reactive Oxygen Intermediates in Atmospheric Aerosol Chemistry. *Phys. Chem. Chem. Phys.* **2016**, *18*, 12662−12674.

(37) Li, Y. J.; Liu, P.; Gong, Z.; Wang, Y.; Bateman, A. P.; Bergoend, C.; Bertram, A. K.; Martin, S. T. Chemical Reactivity and Liquid/Nonliquid States of Secondary Organic Material. *Environ. Sci. Technol.* **2015**, *49*, 13264−13274.
(38) Li, J.; Forrester, S. M.; Knopf, D. A. Heterogeneous Oxidation of Amorphous Organic Aerosol Surrogates by O3, NO3, and OH at Typical Tropospheric Temperatures. *Atmos. Chem. Phys.* **2020**, *20*, 6055−6080.
(39) Zhao, Z.; Tolentino, R.; Lee, J.; Vuong, A.; Yang, X.; Zhang, H. Interfacial Dimerization by Organic Radical Reactions during Heterogeneous Oxidative Aging of Oxygenated Organic Aerosols. *J. Phys. Chem. A* **2019**, *123*, 10782−10792.
(40) Zhou, S.; Shiraiwa, M.; McWhinney, R. D.; Pöschl, U.; Abbatt, J. P. D. Kinetic Limitations in Gas-Particle Reactions Arising from Slow Diffusion in Secondary Organic Aerosol. *Faraday Discuss.* **2013**, *165*, 391−406.
(41) Liu, P.; Li, Y. J.; Wang, Y.; Bateman, A. P.; Zhang, Y.; Gong, Z.; Bertram, A. K.; Martin, S. T. Highly Viscous States Affect the Browning of Atmospheric Organic Particulate Matter. *ACS Cent. Sci.* **2018**, *4*, 207−215.
(42) Chenyakin, Y.; Ullmann, D. A.; Evoy, E.; Renbaum-Wolff, L.; Kamal, S.; Bertram, A. K. Diffusion Coefficients of Organic Molecules in Sucrose-Water Solutions and Comparison with Stokes-Einstein Predictions. *Atmos. Chem. Phys.* **2017**, *17*, 2423−2435.
(43) Evoy, E.; Maclean, A. M.; Rovelli, G.; Li, Y.; Tsimpidi, A. P.; Karydis, V. A.; Kamal, S.; Lelieveld, J.; Shiraiwa, M.; Reid, J. P.; Bertram, A. K. Predictions of Diffusion Rates of Large Organic Molecules in Secondary Organic Aerosols Using the Stokes-Einstein and Fractional Stokes-Einstein Relations. *Atmos. Chem. Phys.* **2019**, *19*, 10073−10085.
(44) Evoy, E.; Kamal, S.; Patey, G. N.; Martin, S. T.; Bertram, A. K. Unified Description of Diffusion Coefficients from Small to Large Molecules in Organic-Water Mixtures. *J. Phys. Chem. A* **2020**, *124*, 2301−2308.
(45) Kiland, K. J.; Maclean, A. M.; Kamal, S.; Bertram, A. K. Diffusion of Organic Molecules as a Function of Temperature in a Sucrose Matrix (a Proxy for Secondary Organic Aerosol). *J. Phys. Chem. Lett.* **2019**, *10*, 5902−5908.
(46) Ullmann, D. A.; Hinks, M. L.; Maclean, A. M.; Butenhoff, C. L.; Grayson, J. W.; Barsanti, K.; Jimenez, J. L.; Nizkorodov, S. A.; Kamal, S.; Bertram, A. K. Viscosities, diffusion coefficients, and mixing times of intrinsic fluorescent organic molecules in brown limonene secondary organic aerosol and tests of the Stokes-Einstein equation. *Atmos. Chem. Phys.* **2019**, *19*, 1491−1503.
(47) Abramson, E.; Imre, D.; Beránek, J.; Wilson, J.; Zelenyuk, A. Experimental Determination of Chemical Diffusion within Secondary Organic Aerosol Particles. *Phys. Chem. Chem. Phys.* **2013**, *15*, 2983−2991.
(48) Price, H. C.; Mattsson, J.; Murray, B. J. Sucrose Diffusion in Aqueous Solution. *Phys. Chem. Chem. Phys.* **2016**, *18*, 19207−19216.
(49) Zhao, Y.; Wingen, L. M.; Perraud, V.; Finlayson-Pitts, B. J. Phase, Composition, and Growth Mechanism for Secondary Organic Aerosol from the Ozonolysis of α-Cedrene. *Atmos. Chem. Phys.* **2016**, *16*, 3245−3264.
(50) Booth, A. M.; Murphy, B.; Riipinen, I.; Percival, C. J.; Topping, D. O. Connecting Bulk Viscosity Measurements to Kinetic Limitations on Attaining Equilibrium for a Model Aerosol Composition. *Environ. Sci. Technol.* **2014**, *48*, 9298−9305.
(51) Hosny, N. A.; Fitzgerald, C.; Tong, C.; Kalberer, M.; Kuimova, M. K.; Pope, F. D. Fluorescent Lifetime Imaging of Atmospheric Aerosols: A Direct Probe of Aerosol Viscosity. *Faraday Discuss.* **2013**, *165*, 343−356.
(52) Song, M.; Liu, P. F.; Hanna, S. J.; Zaveri, R. A.; Potter, K.; You, Y.; Martin, S. T.; Bertram, A. K. Relative Humidity-Dependent Viscosity of Secondary Organic Material from Toluene Photo-Oxidation and Possible Implications for Organic Particulate Matter over Megacities. *Atmos. Chem. Phys.* **2016**, *16*, 8817−8830.
(53) Reid, J. P.; Bertram, A. K.; Topping, D. O.; Laskin, A.; Martin, S. T.; Petters, M. D.; Pope, F. D.; Rovelli, G. The Viscosity of Atmospherically Relevant Organic Particles. *Nat. Commun.* **2018**, *9*, 956.
(54) Shiraiwa, M.; Li, Y.; Tsimpidi, A. P.; Karydis, V. A.; Berkemeier, T.; Pandis, S. N.; Lelieveld, J.; Koop, T.; Pöschl, U. Global Distribution of Particle Phase State in Atmospheric Secondary Organic Aerosols. *Nat. Commun.* **2017**, *8*, 15002.
(55) DeRieux, W.-S. W.; Li, Y.; Lin, P.; Laskin, J.; Laskin, A.; Bertram, A. K.; Nizkorodov, S. A.; Shiraiwa, M. Predicting the Glass Transition Temperature and Viscosity of Secondary Organic Material Using Molecular Composition. *Atmos. Chem. Phys.* **2018**, *18*, 6331−6351.
(56) Gervasi, N. R.; Topping, D. O.; Zuend, A. A Predictive Group-Contribution Model for the Viscosity of Aqueous Organic Aerosol. *Atmos. Chem. Phys.* **2020**, *20*, 2987−3008.
(57) Li, Y.; Day, D. A.; Stark, H.; Jimenez, J. L.; Shiraiwa, M. Predictions of the glass transition temperature and viscosity of organic aerosols from volatility distributions. *Atmos. Chem. Phys.* **2020**, *20*, 8103−8122.
(58) Schmedding, R.; Rasool, Q. Z.; Zhang, Y.; Pye, H. O. T.; Zhang, H.; Chen, Y.; Surratt, J. D.; Lopez-Hilfiker, F. D.; Thornton, J. A.; Goldstein, A. H.; Vizuete, W. Predicting Secondary Organic Aerosol Phase State and Viscosity and Its Effect on Multiphase Chemistry in a Regional-Scale Air Quality Model. *Atmos. Chem. Phys.* **2020**, *20*, 8201−8225.
(59) Ditto, J. C.; Joo, T.; Khare, P.; Sheu, R.; Takeuchi, M.; Chen, Y.; Xu, W.; Bui, A. A. T.; Sun, Y.; Ng, N. L.; Gentner, D. R. Effects of Molecular-Level Compositional Variability in Organic Aerosol on Phase State and Thermodynamic Mixing Behavior. *Environ. Sci. Technol.* **2019**, *53*, 13009.
(60) Schum, S. K.; Zhang, B.; Džepina, K.; Fialho, P.; Mazzoleni, C.; Mazzoleni, L. R. Molecular and Physical Characteristics of Aerosol at a Remote Free Troposphere Site: Implications for Atmospheric Aging. *Atmos. Chem. Phys.* **2018**, *18*, 14017−14036.
(61) Slade, J. H.; Ault, A. P.; Bui, A. T.; Ditto, J. C.; Lei, Z.; Bondy, A. L.; Olson, N. E.; Cook, R. D.; Desrochers, S. J.; Harvey, R. M.; Erickson, M. H.; Wallace, H. W.; Alvarez, S. L.; Flynn, J. H.; Boor, B. E.; Petrucci, G. A.; Gentner, D. R.; Griffin, R. J.; Shepson, P. B. Bouncier Particles at Night: Biogenic Secondary Organic Aerosol Chemistry and Sulfate Drive Diel Variations in the Aerosol Phase in a Mixed Forest. *Environ. Sci. Technol.* **2019**, *53*, 4977−4987.
(62) Riva, M.; Chen, Y.; Zhang, Y.; Lei, Z.; Olson, N. E.; Boyer, H. C.; Narayan, S.; Yee, L. D.; Green, H. S.; Cui, T.; Zhang, Z.; Baumann, K.; Fort, M.; Edgerton, E.; Budisulistiorini, S. H.; Rose, C. A.; Ribeiro, I. O.; e Oliveira, R. L.; Dos Santos, E. O.; Machado, C. M. D.; Szopa, S.; Zhao, Y.; Alves, E. G.; de Sá, S. S.; Hu, W.; Knipping, E. M.; Shaw, S. L.; Duvoisin Junior, S.; De Souza, R. A. F.; Palm, B. B.; Jimenez, J.-L.; Glasius, M.; Goldstein, A. H.; Pye, H. O. T.; Gold, A.; Turpin, B. J.; Vizuete, W.; Martin, S. T.; Thornton, J. A.; Dutcher, C. S.; Ault, A. P.; Surratt, J. D. Increasing Isoprene Epoxydiol-to-Inorganic Sulfate Aerosol Ratio Results in Extensive Conversion of Inorganic Sulfate to Organosulfur Forms: Implications for Aerosol Physicochemical Properties. *Environ. Sci. Technol.* **2019**, *53*, 8682−8694.
(63) Zhang, Y.; Nichman, L.; Spencer, P.; Jung, J. I.; Lee, A.; Heffernan, B. K.; Gold, A.; Zhang, Z.; Chen, Y.; Canagaratna, M. R.; Jayne, J. T.; Worsnop, D. R.; Onasch, T. B.; Surratt, J. D.; Chandler, D.; Davidovits, P.; Kolb, C. E. The Cooling Rate- And Volatility-Dependent Glass-Forming Properties of Organic Aerosols Measured by Broadband Dielectric Spectroscopy. *Environ. Sci. Technol.* **2019**, *53*, 12366−12378.
(64) Wolf, M. J.; Coe, A.; Dove, L. A.; Zawadowicz, M. A.; Dooley, K.; Biller, S. J.; Zhang, Y.; Chisholm, S. W.; Cziczo, D. J. Investigating the Heterogeneous Ice Nucleation of Sea Spray Aerosols UsingProchlorococcusas a Model Source of Marine Organic Matter. *Environ. Sci. Technol.* **2019**, *53*, 1139−1149.
(65) Pratap, V.; Chen, Y.; Yao, G.; Nakao, S. Temperature Effects on Multiphase Reactions of Organic Molecular Markers: A Modeling Study. *Atmos. Environ.* **2018**, *179*, 40−48.
(66) Centeno, G.; Sánchez-Reyna, G.; Ancheyta, J.; Muñoz, J. A. D.; Cardona, N. Testing Various Mixing Rules for Calculation of Viscosity of Petroleum Blends. *Fuel* **2011**, *90*, 3561−3570.

(67) Rovelli, G.; Song, Y.-C.; MacLean, A. M.; Topping, D. O.; Bertram, A. K.; Reid, J. P. Comparison of Approaches for Measuring and Predicting the Viscosity of Ternary Component Aerosol Particles. *Anal. Chem.* **2019**, *91*, 5074−5082.
(68) Song, Y. C.; Haddrell, A. E.; Bzdek, B. R.; Reid, J. P.; Bannan, T.; Topping, D. O.; Percival, C.; Cai, C. Measurements and Predictions of Binary Component Aerosol Particle Viscosity. *J. Phys. Chem. A* **2016**, *120*, 8123−8137.
(69) Champion, W. M.; Rothfuss, N. E.; Petters, M. D.; Grieshop, A. P. Volatility and Viscosity Are Correlated in Terpene Secondary Organic Aerosol Formed in a Flow Reactor. *Environ. Sci. Technol. Lett.* **2019**, *6*, 513−519.
(70) Koop, T.; Bookhold, J.; Shiraiwa, M.; Pöschl, U. Glass Transition and Phase State of Organic Compounds: Dependency on Molecular Properties and Implications for Secondary Organic Aerosols in the Atmosphere. *Phys. Chem. Chem. Phys.* **2011**, *13*, 19238−19255.
(71) Parsons, M. T.; Sydoryk, I.; Lim, A.; McIntyre, T. J.; Tulip, J.; Jäger, W.; McDonald, K. Real-Time Monitoring of Benzene, Toluene, and p-Xylene in a Photoreaction Chamber with a Tunable Mid-Infrared Laser and Ultraviolet Differential Optical Absorption Spectroscopy. *Appl. Opt.* **2011**, *50*, A90.
(72) King, S. M.; Rosenoern, T.; Shilling, J. E.; Chen, Q.; Martin, S. T. Increased Cloud Activation Potential of Secondary Organic Aerosol for Atmospheric Mass Loadings. *Atmos. Chem. Phys.* **2009**, *9*, 2959−2971.
(73) King, S. M.; Rosenoern, T.; Shilling, J. E.; Chen, Q.; Martin, S. T. Cloud Condensation Nucleus Activity of Secondary Organic Aerosol Particles Mixed with Sulfate. *Geophys. Res. Lett.* **2007**, *34*, 1−5.
(74) Kleindienst, T. E.; Smith, D. F.; Li, W.; Edney, E. O.; Driscoll, D. J.; Speer, R. E.; Weathers, W. S. Secondary Organic Aerosol Formation from the Oxidation of Aromatic Hydrocarbons in the Presence of Dry Submicron Ammonium Sulfate Aerosol. *Atmos. Environ.* **1999**, *33*, 3669−3681.
(75) Shilling, J. E.; Chen, Q.; King, S. M.; Rosenoern, T.; Kroll, J. H.; Worsnop, D. R.; McKinney, K. A.; Martin, S. T. Particle mass yield in secondary organic aerosol formed by the dark ozonolysis of α-pinene. *Atmos. Chem. Phys.* **2008**, *8*, 2073−2088.
(76) Kroll, J. H.; Donahue, N. M.; Cee, V. J.; Demerjian, K. L.; Anderson, J. G. Gas-Phase Ozonolysis of Alkenes: Formation of OH from Anti Carbonyl Oxides. *J. Am. Chem. Soc.* **2002**, *124*, 8518−8519.
(77) Tasoglou, A.; Pandis, S. N. Formation and chemical aging of secondary organic aerosol during the β-caryophyllene oxidation. *Atmos. Chem. Phys.* **2015**, *15*, 6035−6046.
(78) Murray, B. J.; Haddrell, A. E.; Peppe, S.; Davies, J. F.; Reid, J. P.; O'Sullivan, D.; Price, H. C.; Kumar, R.; Saunders, R. W.; Plane, J. M. C.; Umo, N. S.; Wilson, T. W. Glass Formation and Unusual Hygroscopic Growth of Iodic Acid Solution Droplets with Relevance for Iodine Mediated Particle Formation in the Marine Boundary Layer. *Atmos. Chem. Phys.* **2012**, *12*, 8575−8587.
(79) Renbaum-Wolff, L.; Grayson, J. W.; Bateman, A. P.; Kuwata, M.; Sellier, M.; Murray, B. J.; Shilling, J. E.; Martin, S. T.; Bertram, A. K. Viscosity of -pinene secondary organic material and implications for particle growth and reactivity. *Proc. Natl. Acad. Sci. U.S.A.* **2013**, *110*, 8014−8019.
(80) Grayson, J. W.; Zhang, Y.; Mutzel, A.; Renbaum-Wolff, L.; Böge, O.; Kamal, S.; Herrmann, H.; Martin, S. T.; Bertram, A. K. Effect of Varying Experimental Conditions on the Viscosity of α-Pinene Derived Secondary Organic Material. *Atmos. Chem. Phys.* **2016**, *16*, 6027−6040.
(81) Martin, S. T. Phase Transitions of Aqueous Atmospheric Particles. *Chem. Rev.* **2000**, *100*, 3403−3454.
(82) Greenspan, L. Humidity Fixed Points of Binary Saturated Aqueous Solutions. *J. Res. Natl. Bur. Stand., Sect. A* **1977**, *81A*, 89.
(83) Reist, P. C. *Aerosol Science and Technology*, 2nd ed.; McGraw-Hill Professional: New York, NY, USA, 1992.
(84) Schneider, C. A.; Rasband, W. S.; Eliceiri, K. W. NIH Image to ImageJ: 25 Years of Image Analysis. *Nat. Methods* **2012**, *9*, 671−675.
(85) Wilson, J.; Imre, D.; Beránek, J.; Shrivastava, M.; Zelenyuk, A. Evaporation Kinetics of Laboratory-Generated Secondary Organic Aerosols at Elevated Relative Humidity. *Environ. Sci. Technol.* **2015**, *49*, 243−249.
(86) Buchholz, A.; Lambe, A. T.; Ylisirniö, A.; Li, Z.; Tikkanen, O. P.; Faiola, C.; Kari, E.; Hao, L.; Luoma, O.; Huang, W.; Mohr, C.; Worsnop, D. R.; Nizkorodov, S. A.; Yli-Juuti, T.; Schobesberger, S.; Virtanen, A. Insights into the O : C-dependent mechanisms controlling the evaporation of α-pinene secondary organic aerosol particles. *Atmos. Chem. Phys.* **2019**, *19*, 4061−4073.
(87) Grayson, J. W.; Song, M.; Sellier, M.; Bertram, A. K. Validation of the Poke-Flow Technique Combined with Simulations of Fluid Flow for Determining Viscosities in Samples with Small Volumes and High Viscosities. *Atmos. Meas. Tech.* **2015**, *8*, 2463−2472.
(88) Roach, P. J.; Laskin, J.; Laskin, A. Nanospray Desorption Electrospray Ionization: An Ambient Method for Liquid-Extraction Surface Sampling in Mass Spectrometry. *Analyst* **2010**, *135*, 2233−2236.
(89) Nizkorodov, S. A.; Laskin, J.; Laskin, A. Molecular Chemistry of Organic Aerosols through the Application of High Resolution Mass Spectrometry. *Phys. Chem. Chem. Phys.* **2011**, *13*, 3612−3629.
(90) Leenheer, J. A.; Rostad, C. E.; Gates, P. M.; Furlong, E. T.; Ferrer, I. Molecular Resolution and Fragmentation of Fulvic Acid by Electrospray Ionization/Multistage Tandem Mass Spectrometry. *Anal. Chem.* **2001**, *73*, 1461−1471.
(91) Willoughby, R.; Sheehan, E.; Mitrovich, S. *A Global View of LC/MS*; Global View Publishing: Pittsburg, 1998.
(92) Song, M.; Maclean, A. M.; Huang, Y.; Smith, N. R.; Blair, S. L.; Laskin, J.; Laskin, A.; DeRieux, W.-S. W.; Li, Y.; Shiraiwa, M.; Nizkorodov, S. A.; Bertram, A. K. Liquid-Liquid Phase Separation and Viscosity within Secondary Organic Aerosol Generated from Diesel Fuel Vapors. *Atmos. Chem. Phys.* **2019**, *19*, 12515−12529.
(93) Zobrist, B.; Marcolli, C.; Pedernera, D. A.; Koop, T. Do Atmospheric Aerosols Form Glasses? *Atmos. Chem. Phys.* **2008**, *8*, 5221−5244.
(94) Kohl, I.; Bachmann, L.; Hallbrucker, A.; Mayer, E.; Loerting, T. Liquid-like relaxation in hyperquenched water at ≤140 K. *Phys. Chem. Chem. Phys.* **2005**, *7*, 3210−3220.
(95) Petters, M. D.; Kreidenweis, S. M. A Single Parameter Representation of Hygroscopic Growth and Cloud Condensation Nucleus Activity. *Atmos. Chem. Phys.* **2007**, *7*, 1961−1971.
(96) Asa-Awuku, A.; Engelhart, G. J.; Lee, B. H.; Pandis, S. N.; Nenes, A. Relating CCN activity, volatility, and droplet growth kinetics of β-caryophyllene secondary organic aerosol. *Atmos. Chem. Phys.* **2009**, *9*, 795−812.
(97) Frosch, M.; Bilde, M.; Nenes, A.; Praplan, A. P.; Jurányi, Z.; Dommen, J.; Gysel, M.; Weingartner, E.; Baltensperger, U. CCN activity and volatility of β-caryophyllene secondary organic aerosol. *Atmos. Chem. Phys.* **2013**, *13*, 2283−2297.
(98) Angell, C. A. Relaxation in Liquids, Polymers and Plastic Crystals - Strong/Fragile Patterns and Problems. *J. Non-Cryst. Solids* **1991**, *131*−*133*, 13−31.
(99) Angell, C. A. Liquid Fragility and the Glass Transition in Water and Aqueous Solutions. *Chem. Rev.* **2002**, *102*, 2627−2650.
(100) Rothfuss, N. E.; Petters, M. D. Influence of Functional Groups on the Viscosity of Organic Aerosol. *Environ. Sci. Technol.* **2017**, *51*, 271−279.
(101) Marsh, A.; Petters, S. S.; Rothfuss, N. E.; Rovelli, G.; Song, Y. C.; Reid, J. P.; Petters, M. D. Amorphous Phase State Diagrams and Viscosity of Ternary Aqueous Organic/Organic and Inorganic/Organic Mixtures. *Phys. Chem. Chem. Phys.* **2018**, *20*, 15086−15097.
(102) Rothfuss, N. E.; Petters, M. D. Characterization of the Temperature and Humidity-Dependent Phase Diagram of Amorphous Nanoscale Organic Aerosols. *Phys. Chem. Chem. Phys.* **2017**, *19*, 6532−6545.
(103) Longinotti, M. P.; Corti, H. R. Viscosity of Concentrated Sucrose and Trehalose Aqueous Solutions Including the Supercooled Regime. *J. Phys. Chem. Ref. Data* **2008**, *37*, 1503−1515.
(104) Kasparoglu, S.; Li, Y.; Shiraiwa, M.; Petters, M. Toward Closure between Predicted and Observed Particle Viscosity over a Wide Range Temperature and Relative Humidity. *Atmos. Chem. Phys. Discuss.* **2020**, 1−22.

https://dx.doi.org/10.1021/acsearthspacechem.0c00296
ACS Earth Space Chem. 2021, 5, 305−318

(105) Zhmud, B. Viscosity Blending Equations. *Lube Mag* **2014**, *121*, 22−27.
(106) Crittenden, J. C.; Trussel, R. R.; Hand, D. W.; Howe, K. J.; Tchobanoglous, G. *MWH's Water Treatment*; John Wiley and Sons, 2012.
(107) Ruiz, L. H.; Paciga, A. L.; Cerully, K. M.; Nenes, A.; Donahue, N. M.; Pandis, S. N. Formation and Aging of Secondary Organic Aerosol from Toluene: Changes in Chemical Composition, Volatility, and Hygroscopicity. *Atmos. Chem. Phys.* **2015**, *15*, 8301−8313.
(108) Pajunoja, A.; Lambe, A. T.; Hakala, J.; Rastak, N.; Cummings, M. J.; Brogan, J. F.; Hao, L.; Paramonov, M.; Hong, J.; Prisle, N. L.; Malila, J.; Romakkaniemi, S.; Lehtinen, K. E. J.; Laaksonen, A.; Kulmala, M.; Massoli, P.; Onasch, T. B.; Donahue, N. M.; Riipinen, I.; Davidovits, P.; Worsnop, D. R.; Petäjä, T.; Virtanen, A. Adsorptive Uptake of Water by Semisolid Secondary Organic Aerosols. *Geophys. Res. Lett.* **2015**, *42*, 3063−3068.
(109) Easteal, A. J. Tracer Diffusion in Aqueous Sucrose and Urea Solutions. *Can. J. Chem.* **1990**, *68*, 1611−1615.
(110) Li, Y. J.; Chen, Q.; Guzman, M. I.; Chan, C. K.; Martin, S. T. Second-generation products contribute substantially to the particle-phase organic material produced by β-caryophyllene ozonolysis. *Atmos. Chem. Phys.* **2011**, *11*, 121−132.
(111) Cheng, Y.; Su, H.; Koop, T.; Mikhailov, E.; Pöschl, U. Size Dependence of Phase Transitions in Aerosol Nanoparticles. *Nat. Commun.* **2015**, *6*, 5923.
(112) Mattsson, J.; Forrest, J. A.; Börjesson, L. Quantifying Glass Transition Behavior in Ultrathin Free-Standing Polymer Films. *Phys. Rev. E: Stat. Phys., Plasmas, Fluids, Relat. Interdiscip. Top.* **2000**, *62*, 5187−5200.
(113) Alcoutlabi, M.; McKenna, G. B. Effects of Confinement on Material Behaviour at the Nanometre Size Scale. *J. Phys. Condens. Matter* **2005**, *17*, R461.
(114) Martin, S. T.; Andreae, M. O.; Althausen, D.; Artaxo, P.; Baars, H.; Borrmann, S.; Chen, Q.; Farmer, D. K.; Guenther, A.; Gunthe, S. S.; Jimenez, J. L.; Karl, T.; Longo, K.; Manzi, A.; Müller, T.; Pauliquevis, T.; Petters, M. D.; Prenni, A. J.; Pöschl, U.; Rizzo, L. V.; Schneider, J.; Smith, J. N.; Swietlicki, E.; Tota, J.; Wang, J.; Wiedensohler, A.; Zorn, S. R. An Overview of the Amazonian Aerosol Characterization Experiment 2008 (AMAZE-08). *Atmos. Chem. Phys.* **2010**, *10*, 11415−11438.
(115) Pöschl, U.; Martin, S. T.; Sinha, B.; Chen, Q.; Gunthe, S. S.; Huffman, J. A.; Borrmann, S.; Farmer, D. K.; Garland, R. M.; Helas, G.; Jimenez, J. L.; King, S. M.; Manzi, A.; Mikhailov, E.; Pauliquevis, T.; Petters, M. D.; Prenni, A. J.; Roldin, P.; Rose, D.; Schneider, J.; Su, H.; Zorn, S. R.; Artaxo, P.; Andreae, M. O. Rainforest Aerosols as Biogenic Nuclei of Clouds and Precipitation in the Amazon. *Science* **2010**, *329*, 1513−1516.
(116) Riipinen, I.; Pierce, J. R.; Yli-Juuti, T.; Nieminen, T.; Häkkinen, S.; Ehn, M.; Junninen, H.; Lehtipalo, K.; Petäjä, T.; Slowik, J.; Chang, R.; Shantz, N. C.; Abbatt, J.; Leaitch, W. R.; Kerminen, V.-M.; Worsnop, D. R.; Pandis, S. N.; Donahue, N. M.; Kulmala, M. Organic Condensation: A Vital Link Connecting Aerosol Formation to Cloud Condensation Nuclei (CCN) Concentrations. *Atmos. Chem. Phys.* **2011**, *11*, 3865−3878.
(117) Maclean, A. M.; Butenhoff, C. L.; Grayson, J. W.; Barsanti, K.; Jimenez, J. L.; Bertram, A. K. Mixing Times of Organic Molecules within Secondary Organic Aerosol Particles: A Global Planetary Boundary Layer Perspective. *Atmos. Chem. Phys.* **2017**, *17*, 13037−13048.
(118) Raatikainen, T.; Vaattovaara, P.; Tiitta, P.; Miettinen, P.; Rautiainen, J.; Ehn, M.; Kulmala, M.; Laaksonen, A.; Worsnop, D. R. Physicochemical properties and origin of organic groups detected in boreal forest using an aerosol mass spectrometer. *Atmos. Chem. Phys.* **2010**, *10*, 2063−2077.
(119) Jain, S.; Fischer, K. B.; Petrucci, G. A. The Influence of Absolute Mass Loading of Secondary Organic Aerosols on Their Phase State. *Atmosphere* **2018**, *9*, 131.
(120) Donahue, N. M.; Robinson, A. L.; Pandis, S. N. Atmospheric Organic Particulate Matter: From Smoke to Secondary Organic Aerosol. *Atmos. Environ.* **2009**, *43*, 94−106.
(121) Ye, Q.; Upshur, M. A.; Robinson, E. S.; Geiger, F. M.; Sullivan, R. C.; Thomson, R. J.; Donahue, N. M.; Ye, Q.; Upshur, M. A.; Robinson, E. S.; Geiger, F. M.; Sullivan, R. C.; Thomson, R. J.; Donahue, N. M. Following Particle-Particle Mixing in Atmospheric Secondary Organic Aerosols by Using Isotopically Labeled Terpenes. *Chem* **2018**, *4*, 318−333.
(122) Roach, P. J.; Laskin, J.; Laskin, A. Molecular Characterization of Organic Aerosols Using Nanospray-Desorption/Electrospray Ionization-Mass Spectrometry†. *Anal. Chem.* **2010**, *82*, 7979−7986.
(123) Laskin, J.; Laskin, A.; Roach, P. J.; Slysz, G. W.; Anderson, G. A.; Nizkorodov, S. A.; Bones, D. L.; Nguyen, L. Q. High-Resolution Desorption Electrospray Ionization Mass Spectrometry for Chemical Characterization of Organic Aerosols. *Anal. Chem.* **2010**, *82*, 2048−2058.
(124) Klodt, A. L.; Romonosky, D. E.; Lin, P.; Laskin, J.; Laskin, A.; Nizkorodov, S. A. Aqueous Photochemistry of Secondary Organic Aerosol of α-Pinene and α-Humulene in the Presence of Hydrogen Peroxide or Inorganic Salts. *ACS Earth Space Chem.* **2019**, *3*, 2736−2746.
(125) Romonosky, D. E.; Li, Y.; Shiraiwa, M.; Laskin, A.; Laskin, J.; Nizkorodov, S. A. Aqueous Photochemistry of Secondary Organic Aerosol of α-Pinene and α-Humulene Oxidized with Ozone, Hydroxyl Radical, and Nitrate Radical. *J. Phys. Chem. A* **2017**, *121*, 1298−1309.
(126) Jaoui, M.; Kamens, R. M. Gas and Particulate Products Distribution from the Photooxidation of α-Humulene in the Presence of NOx, Natural Atmospheric Air and Sunlight. *J. Atmos. Chem.* **2003**, *46*, 29−54.
(127) Richters, S.; Herrmann, H.; Berndt, T. Different Pathways of the Formation of Highly Oxidized Multifunctional Organic Compounds (HOMs) from the Gas-Phase Ozonolysis of β-Caryophyllene. *Atmos. Chem. Phys.* **2016**, *16*, 9831−9845.
(128) Kenseth, C. M.; Hafeman, N. J.; Huang, Y.; Dalleska, N. F.; Stoltz, B. M.; Seinfeld, J. H. Synthesis of Carboxylic Acid and Dimer Ester Surrogates to Constrain the Abundance and Distribution of Molecular Products in α-Pinene and β-Pinene Secondary Organic Aerosol. *Environ. Sci. Technol.* **2020**, *54*, 12829.
(129) Nguyen, T. B.; Nizkorodov, S. A.; Laskin, A.; Laskin, J. An Approach toward Quantification of Organic Compounds in Complex Environmental Samples Using High-Resolution Electrospray Ionization Mass Spectrometry. *Anal. Methods* **2013**, *5*, 72−80.

https://dx.doi.org/10.1021/acsearthspacechem.0c00296
ACS Earth Space Chem. 2021, 5, 305−318